An empirical algorithm to map perennial firn aquifers and ice slabs within the Greenland Ice Sheet using satellite L-band microwave radiometry

Julie Z. Miller[1,2], Riley Culberg[3], David G. Long[4], Christopher A. Shuman[5], Dustin M. Schroeder[3,6], Mary J. Brodzik[1,7]

[1]Cooperative Institute for Research in Environmental Sciences, University of Colorado, Boulder, Colorado, USA
[2]Earth Science and Observation Center, University of Colorado, Boulder, Colorado, USA
[3]Department of Electrical Engineering, Stanford University, Stanford, California, USA
[4]Department of Electrical and Computer Engineering, Brigham Young University, Provo, Utah, USA
[5]University of Maryland, Baltimore County, Joint Center for Earth Systems Technology at Code 615, Cryospheric Sciences Laboratory NASA Goddard Space Flight Center, Greenbelt, Maryland, USA
[6]Department of Geophysics, Stanford University, Stanford, CA, USA
[7]National Snow and Ice Data Center, University of Colorado, Boulder, Colorado, USA

Correspondence to: jzmiller.research@gmail.com

Abstract

Perennial firn aquifers are subsurface meltwater reservoirs consisting of a meters-thick water-saturated firn layer that can form on spatial scales as large as tens of kilometers. They have been observed within the percolation facies of glaciated regions experiencing intense seasonal surface melting and high snow accumulation. Widespread perennial firn aquifers have been identified within the Greenland Ice Sheet (GrIS) via field expeditions, airborne ice-penetrating radar surveys, and satellite microwave sensors. In contrast, ice slabs are nearly-continuous ice layers that can also form on spatial scales as large as tens of kilometers as a result of surface and subsurface water-saturated snow and firn layers sequentially refreezing following multiple melting seasons. They have been observed within the percolation facies of glaciated regions experiencing intense seasonal surface melting, but in areas where snow accumulation is at least 25% lower as compared to perennial firn aquifer areas. Widespread ice slabs have recently been identified within the GrIS via field expeditions and airborne ice-penetrating radar surveys, specifically in areas where perennial firn aquifers typically do not form. However, ice slabs have yet to be identified from space. Together, these two ice sheet features represent distinct, but related, sub-facies within the broader percolation facies of the GrIS that can be defined primarily by differences in snow accumulation, which influences the englacial hydrology and thermal characteristics of firn layers at depth.

Here, for the first time, we use enhanced-resolution vertically-polarized L-band brightness temperature (T_V^B) imagery (2015-2019) generated using observations collected over the GrIS by NASA's Soil Moisture Active Passive (SMAP) satellite to map perennial firn aquifer and ice slab areas together as a continuous englacial hydrological system. We use an empirical algorithm previously developed to map the extent of Greenland's perennial firn aquifers via fitting exponentially decreasing temporal L-band signatures to a set of sigmoidal curves. This algorithm is recalibrated to also map the extent of ice slab areas using airborne ice-penetrating radar surveys collected by NASA's Operation Ice Bridge (OIB) campaigns (2010-2017). Our SMAP-derived maps

show that between 2015 and 2019, perennial firn aquifer areas extended over 64,000 km², and ice slab areas extended over 76,000 km². Combined together, these sub-facies are the equivalent of 24% of the percolation facies of the GrIS. As Greenland's climate continues to warm, seasonal surface melting will increase in extent, intensity, and duration. Quantifying the possible rapid expansion of these sub-facies using satellite L-band microwave radiometry has significant implications for understanding ice sheet-wide variability in englacial firn hydrology resulting in meltwater-induced hydrofracturing and accelerated ice flow as well as high-elevation meltwater run-off that can impact the mass balance and stability of the GrIS.

1 Introduction

The recent launches of several satellite L-band microwave radiometry missions by NASA (Aquarius mission, Levine, et al., 2007; Soil Moisture Active Passive (SMAP) mission, Entekhabi et al., 2010) and ESA (Soil Moisture and Ocean Salinity (SMOS), Kerr et al., 2010) have provided a new Earth-observation tool capable of detecting meltwater stored tens of meters to kilometers beneath the ice sheet surface. Jezek et al. (2015) recently demonstrated that in the high-elevation (3500 m a.s.l.) dry snow facies of the Antarctic Ice Sheet, meltwater stored in subglacial Lake Vostok can be detected as deep as 4 km beneath the ice sheet surface. Subglacial lakes represent radiometrically cold subsurface meltwater reservoirs. Upwelling L-band emission from the radiometrically warm bedrock underlying the subglacial lakes is effectively blocked by high reflectivity and attenuation at the interface between the bedrock and the overlying lake bottom. This results in a lower observed microwave brightness temperature (T^B) at the ice sheet surface as compared to other dry snow facies areas where bedrock contributes to L-band emission depth-integrated over the entire ice sheet thickness.

Similar to subglacial lakes, perennial firn aquifers also represent radiometrically cold subsurface meltwater reservoirs (Miller et al., 2020) consisting of a 4-25 m thick water-saturated firn layer (Koenig et al., 2014; Montgomery et al., 2017; Chu et al., 2018) that can form on spatial scales as large as tens of kilometers (Forster et al., 2014). Perennial firn aquifers have been identified via field expeditions (Forster et al., 2014), airborne ice-penetrating radar surveys (Miege et al., 2016), and satellite microwave sensors (Brangers et al., 2020; Miller et al., 2020) in the lower-elevation (<2000 m a.s.l.) percolation facies of the Greenland Ice Sheet (GrIS) at depths from between 1 m and 40 m beneath the ice sheet surface. They exist in areas that experience intense seasonal surface melting and rain (>650 mm w.e. yr^{-1}) during the melting season and high snow accumulation (>800 mm w.e. yr^{-1}) during the freezing season (Forster et al., 2014). High snow accumulation in perennial firn aquifer areas thermally insulates water-saturated firn layers from the cold atmosphere allowing seasonal meltwater to be stored in liquid form year-round if the overlying seasonal snow layer is sufficiently thick (Kuipers Munneke et al., 2014). Koenig et al. (2014) estimated that the volumetric fraction of meltwater stored within the pore space of Greenland's perennial firn aquifers just prior to melt onset ranges from between 10% and 25%, which limits the upward propagation of electromagnetic energy from greater depths within the ice sheet. Large volumetric fractions of meltwater within the firn pore space results in high reflectivity and attenuation at the interface between water-saturated

78 firn layers and the overlying refrozen firn layers, and between glacial ice or an impermeable layer and the
79 overlying water-saturated firn layers. Upwelling L-band emission from deeper glacial ice and the underlying
80 bedrock is effectively blocked.
81 While perennial firn aquifers are radiometrically cold, the slow refreezing of deeper firn layers
82 saturated with large volumetric fractions of meltwater represents a significant source of latent heat that is
83 continuously released throughout the freezing season. Refreezing of seasonal meltwater by the descending
84 winter cold wave (Pfeffer et al., 1991), and the subsequent formation of embedded ice structures (i.e.,
85 horizontally-oriented ice layers and ice lenses, and vertically-oriented ice pipes; Benson et al., 1960;
86 Humphrey et al., 2012; Harper et al., 2012) within the upper snow and firn layers represents a secondary
87 source of latent heat. These heat sources help maintain meltwater at depth. Perennial firn aquifer areas
88 are radiometrically warmer than other percolation facies areas where the single source of latent heat is via
89 refreezing of seasonal meltwater. This results in a higher observed T^B at the ice sheet surface during the
90 freezing season as compared to other percolation facies areas where seasonal meltwater is fully refrozen
91 and stored exclusively as embedded ice.
92 Recently, mapping the extent of Greenland's perennial firn aquifers from space was demonstrated
93 using satellite L-band microwave radiometry (Miller et al., 2020). Exponentially decreasing temporal L-band
94 signatures observed in enhanced-resolution vertically-polarized L-band brightness temperature (T_V^B)
95 imagery (2015-2016) generated using observations collected over the GrIS by the microwave radiometer
96 on NASA's SMAP satellite (Long et al., 2019) were correlated with a single year of perennial firn aquifer
97 detections (Miège et al. 2016). These detections were identified via the Center for Remote Sensing of Ice
98 Sheets (CReSIS) Multi-Channel Coherent Radar Depth Sounder (MCoRDS) flown by NASA's Operation
99 Ice Bridge (OIB) campaigns (Rodriguez-Morales et al, 2014). An empirical algorithm to map extent was
100 developed by fitting temporal L-band signatures to a set of sigmoidal curves derived from the continuous
101 logistic model.
102 The relationship between the radiometric, and thus the physical, temperature of perennial firn
103 aquifer areas, as compared to other percolation facies areas, forms the basis of the empirical algorithm.
104 Miller et al. (2020) hypothesized that the dominant control on the relatively slow exponential rate of T^B
105 decrease over perennial firn aquifer areas is physical temperature versus depth. L-band emission from the
106 radiometrically warm upper snow and firn layers decreases during the freezing season as embedded ice
107 structures slowly refreeze at increased depths below the ice sheet surface. In the percolation facies,
108 refreezing of seasonal meltwater results in the formation of an intricate network of embedded ice structures
109 that are large (10-100 cm long, 10-20 cm wide; Jezek et al., 1994) relative to the L-band wavelength (21
110 cm). Embedded ice structures induce strong volume scattering (Rignot et al., 1993; Rignot 1995) that
111 decreases T^B (Zwally, 1977; Swift et al. 1985; Jezek et al., 2018).
112 Ice slabs are 1-16 m thick nearly-continuous ice layers that that can form on spatial scales as large
113 as tens of kilometers as a result of surface and subsurface water-saturated snow and firn layers sequentially
114 refreezing following multiple melting seasons (Machguth et al., 2016; MacFerrin et al., 2019). Over time,

they become dense low-permeability solid-ice layers overlying deeper permeable firn layers. Ice slabs have been identified via field expeditions and airborne ice-penetrating radar surveys in the lower-elevation (<2000 m a.s.l.) percolation facies of the GrIS at depths from between 1 m and 20 m beneath the ice sheet surface (MacFerrin et al., 2019). They exist in areas that experience intense seasonal surface melting and rain (266-573 mm w.e. yr−1) during the melting season, and lower snow accumulation (<572+/-32 mm w.e. yr−1) during the freezing season as compared to perennial firn aquifer areas (MacFerrin et al., 2019). Lower snow accumulation in ice slab areas results in a seasonal snow layer that is insufficiently thick to thermally insulate water-saturated firn layers and seasonal meltwater is instead stored as embedded ice. Refreezing of seasonal meltwater by the descending winter cold wave, and the subsequent formation of ice slabs as well as other embedded ice structures within the upper snow and firn layers is the single source of latent heat. While ice slab areas are radiometrically warmer than other percolation facies areas with a lower volumetric fraction of embedded ice, they are radiometrically colder than perennial firn aquifer areas. This results in typically higher observed T^B at the ice sheet surface during the freezing season in ice slab areas, as compared to other percolation facies areas, however, typically lower observed T^B as compared to perennial firn aquifer areas. Similar to temporal L-band signatures over perennial firn aquifer areas, temporal L-band signatures over ice slab areas are exponentially decreasing during the freezing season, however, the rate of T^B decrease is slightly more rapid.

In this study, we exploit the observed sensitivity of L-band emission to differences in the depth- and time-integrated dielectric and geophysical properties of the percolation facies of the GrIS to map perennial firn aquifer and ice slab areas together as a continuous englacial firn hydrological system using satellite L-band microwave radiometry

2 Methods

We adapt our previously developed empirical algorithm to map the extent of Greenland's perennial firn aquifers (Miller et al., 2020) using a multi-year calibration technique. We use enhanced-resolution L-band T_V^B imagery (2015-2019) generated using observations collected over the GrIS by the microwave radiometer on NASA's SMAP satellite (Long et al., 2019) and airborne ice-penetrating radar surveys collected by NASA's OIB campaigns (Rodriguez-Morales et al, 2014). First, we correlate: (1) a 'firn saturation' parameter derived from a simple two-layer L-band brightness temperature model (Miller et al., 2021, in press), (2) maximum and (3) minimum T_V^B values, and (4) exponentially decreasing temporal L-band signatures, with five years of perennial firn aquifer detections (2010-2014) identified via the CReSIS Accumulation Radar (AR) (Miège et al. 2016), and three years of additional detections (2015-2017) more recently identified via MCoRDS (Miller et al., 2020). Next, we extend our empirical algorithm to map the extent of ice slab areas. We correlate the SMAP-derived parameters with five years of ice slab detections (2010-2014) recently identified via AR (MacFerrin et al., 2019). Finally, were re-calibrate our empirical model to map the extent of perennial firn aquifer and ice slab areas over the percolation facies. Interannual variability in extent is not resolved in this study, however, it will be explored further in future work.

2.1 SMAP Enhanced-Resolution L-band T^B Imagery

The key science objectives of NASA's SMAP mission (https://smap.jpl.nasa.gov/) are to map terrestrial soil moisture and freeze/thaw state over Earth's land surfaces from space. However, the global L-band T^B observations collected by the SMAP satellite also have cryospheric applications. Mapping perennial firn aquifer and ice slab areas over Earth's polar ice sheets represents an interesting analog and an innovative extension of the science objectives. The SMAP satellite was launched 31 January 2015 and carries a microwave radiometer that operates at an L-band frequency of 1.41 GHz (Enkentabi et al., 2010). It is currently collecting observations of vertically and horizontally-polarized T^B over Greenland. The surface incidence angle is 40°, and the radiometric accuracy is approximately 1.3 K (Piepmeier et al., 2017).

The Scatterometer Image Reconstruction (SIR) algorithm was originally developed to reconstruct coarse resolution satellite radar scatterometry imagery on a higher spatial resolution grid (Long et al., 1993; Early and Long, 2001). The SIR algorithm has been adapted for coarse resolution satellite microwave radiometry imagery (Long and Daum, 1998; Long and Brodzik, 2016; Long et al., 2019). The microwave radiometer form of the SIR algorithm (rSIR) uses the measurement response function (MRF) for each observation, which is a smeared version of the antenna pattern. Using the overlapping MRFs, the rSIR algorithm reconstructs T^B from the spatially filtered low-resolution sampling provided by the observations. In effect, it generates an MRF-deconvolved T^B image. Combining multiple orbital passes increases the sampling density, which improves both the accuracy and resolution of the SMAP enhanced-resolution T^B imagery (Long et al., 2019).

Over Greenland, the rSIR algorithm combines satellite orbital passes that occur between 8 a.m. and 4 p.m. local time-of-day to reconstruct SMAP enhanced-resolution T^B imagery twice-daily (i.e., morning and evening orbital pass interval, respectively). T^B imagery is projected on a Northern Hemisphere (NH) Equal-Area Scalable Earth Grid (EASE-Grid 2.0; Brodzik et al., 2012) at a 3.125 km rSIR grid cell spacing (e.g., Fig. 1). The effective resolution for each grid cell is dependent on the number of observations used in the rSIR reconstruction and is coarser than the rSIR grid cell spacing. While the effective resolution of conventionally processed SMAP T^B imagery posted on a 25 km grid is approximately 30 km (e.g., Fig. 1a), the effective resolution of SMAP enhanced-resolution T^B imagery posted on a 3.125 km grid is approximately 18 km (e.g., Fig. 1b), an improvement of 60% (Long et al., 2020).

As previously noted, for our analysis of the percolation facies we use SMAP enhanced-resolution T_V^B imagery over the GrIS. Compared to the horizontally-polarized channel, the vertically-polarized channel exhibits decreased sensitivity to variability in the volumetric fraction of meltwater, which is attributed to reflection coefficient differences between channels (Miller et al., 2020). Using the vertically polarized channel also results in a reduced chi-squared error statistic when fitting T_V^B time series to the sigmoid function (Section 2.3.4). We construct T_V^B imagery that alternate morning and evening orbital pass observations annually, beginning and ending just prior to melt onset. The Greenland Ice Mapping Project (GIMP) Land Ice and Ocean Classification Mask and Digital Elevation Model (Howat et al., 2014) are projected on the NH EASE-Grid 2.0 at a 3.125 km rSIR grid cell spacing. T_V^B imagery between 1 April 2015

and 31 March 2019 are ice sheet-masked, and an elevation for each rSIR grid cell is calculated.

2.2 Airborne Ice-Penetrating Radar Surveys

AR and MCoRDS (Rodriguez-Morales et al, 2014) were flown over the GrIS on a P-3 aircraft in April and May between 2010 and 2017 (Figs. 1c; 2). The AR instrument operates at a center frequency of 750 MHz with a bandwidth of 300 MHz, resulting in a range resolution in firn of 0.53 m (Lewis et al., 2015). The collected data have an along-track resolution of approximately 30 m with 15 m spacing between traces in the final processed radargrams. At a nominal flight altitude of 500 m above the ice sheet surface, the cross-track resolution varies between 20 m for a smooth surface, to 54 m for a rough surface with no appreciable layover. The MCoRDS instrument operated at three different frequency configurations: (1) a center with a bandwidth of 30 MHz (2010-2014, 2017, 2018), (2) a center frequency of 315 MHz with a band width of 270 MHz (2015), and (3) a center frequency of 300 MHz with a bandwidth of 300 MHz (2016). The vertical range resolution in firn for each of these frequency configurations is 5.3 m, 0.59 m, and 0.53m, respectively (CReSIS, 2016). The collected data have an along-track resolution of approximately 25 m with 14 m spacing between traces in the final processed radargrams. At a nominal flight altitude of 500 m, the cross-track resolution varies between 40 m for a smooth surface in the highest bandwidth configuration, to 175 m for a rough surface with no appreciable layover in the lowest bandwidth configuration.

The multi-year calibration technique uses perennial firn aquifer detections previously identified along OIB flight lines via AR (2010-2014) and MCoRDS (2015-2017) radargram profiles and the methodology described in Miège et al. (2016). Bright lower reflectors that undulate with the local topographic gradient underneath which reflectors are absent in the percolation facies are interpreted as the upper surface of meltwater stored within perennial firn aquifers (e.g., Fig. 3a). The large dielectric contrast between refrozen and water-saturated firn layers results in high reflectivity at the interface. However, the presence of meltwater increases attenuation, limiting the downward propagation of electromagnetic energy through the water-saturated firn layer. The total number of AR derived perennial firn aquifer detections is 325,000, corresponding to a total extent of 98 km^2. The analysis assumes a smooth surface, which is typical of much of the percolation facies, and a grid cell size of 15 m x 20 m. The total number of MCoRDS-derived perennial firn aquifer detections is 142,000, corresponding to a total extent of 80 km^2. This analysis also assumes a smooth surface, and a grid cell size of 14 m x 40 m. The combined total number of grid cells (467,000) and total extent (178 km^2) is significantly larger than the total number of MCoRDS-derived grid cells (78,000) and total extent (44 km^2) calculated for 2016 (Miller et al., 2020). Perennial firn aquifer detections are mapped in western, southern, and south and central eastern Greenland as well as the Maniitsoq and Flade Isblink Ice Caps (Figs. 1c; 2a). We project AR- and MCoRDS-derived perennial firn aquifer detections on the NH EASE-Grid 2.0 at an rSIR grid cell spacing of 3.125 km. Each rSIR grid cell has an extent of approximately 10 km^2. The total number of rSIR grid cells with at least one perennial firn aquifer detection is 800, corresponding to a total extent of 8000 km^2. However, given the limited AR and MCoRDS grid cell coverage, less than 1% of the rSIR grid cell extent has airborne ice-penetrating radar survey coverage. As compared to the total number of MCoRDS-derived perennial firn aquifer detections

(780) calculated for 2016 (Miller et al., 2020), the total number of rSIR grid cells with at least one detection is only increased by 20 for the multi-year calibration technique, corresponding to an increased total extent of 200 km^2.

We also use ice slab detections previously identified along OIB flight lines via AR (2010-2014) radargram profiles and the methodology described in MacFerrin et al. (2019) in the multi-year calibration technique. Thick dark surface-parallel regions of low-reflectivity in the percolation facies are interpreted as ice slabs (e.g., Fig. 3b). The large dielectric contrast between ice slabs and the overlying and underlying snow and firn layers results in high reflectivity at the interfaces. However, electromagnetic energy is not scattered or absorbed within the homogeneous ice slab, it instead propagates downward through the layer and into the deeper firn layers. The total number of AR-derived ice slab detections is 505,000, corresponding to a total extent of 283 km^2. Ice slab detections are mapped in western, central and north eastern, and northern Greenland as well as the Flade Isblink Ice Cap (Figs. 1c; 2b). We project the AR-derived ice slab detections on the NH EASE-Grid 2.0 at an rSIR grid cell spacing of 3.125 km. The total number of rSIR grid cells with at least one ice slab detection is 2000, corresponding to a total extent of 20,000 km^2. However, less than 2% of the rSIR grid cell extent has airborne ice-penetrating radar survey coverage.

An advantage of the multi-year calibration technique as compared to the single-coincident year calibration technique (Miller et al., 2020) is that it increases the number of rSIR grid cells that can be assessed. It also provides repeat targets that can account for variability in the depth- and time-integrated dielectric and geophysical properties that influence the radiometric temperature in stable perennial firn aquifer and ice slab areas. Uncertainty is introduced by correlating the SMAP-derived parameters with AR- and MCoRDS-derived detections that are not coincident in time. The multi-year calibration technique assumes the extent of each area remains stable, which is not necessarily the case as climate extremes (Cullather et al., 2020) can influence each of these sub-facies. The assumption of stability neglects boundary transitions in the extent of perennial firn aquifer areas associated with refreezing of shallow water-saturated firn layers, englacial drainage of meltwater into crevasses at the periphery (Poinar et al., 2017; Poinar et al, 2019), and transient upslope expansion (Montgomery et al., 2017). Once formed, ice slabs are essentially permanent features within the upper snow and firn layers of the percolation facies until they are compressed into glacial ice. However, they may transition into superimposed ice at the lower boundary of ice slab areas or rapidly expand upslope, particularly following extreme melting seasons (MacFerrin et al., 2019). Thus, we simply consider our mapped extent a high-probability area for the preferential formation of each of these sub-facies, with continued presence dependent on seasonal surface melting and snow accumulation in subsequent years.

Annual perennial firn aquifer and ice slab detections that may introduce significant uncertainty into the multi-year calibration technique include those following the 2010 melting season, which was exceptionally long (Tedesco et al., 2010), the anomalous 2012 melting season, during which seasonal surface melting extended across 99% of the GrIS (Nghiem et al., 2012), and the 2015 melting season,

which was especially intense in western and northern Greenland (Tedesco et al., 2016). Following these extreme melting seasons, significant changes in the dielectric and geophysical properties likely occurred across large portions of the GrIS, including perennial firn aquifer recharging resulting in increases in meltwater volume and decreases in the depth to the upper surface of stored meltwater. The upper snow and firn layers of the dry snow facies and percolation facies were also saturated with relatively large volumetric fractions of meltwater as compared to the negligible to limited volumetric fractions of meltwater that percolates during more typical seasonal surface melting on the GrIS.

Seasonal meltwater was refrozen into spatially coherent melt layers following the 2010 and 2012 melting seasons (Culberg et al., 2021) as well as more recently following the 2015, and 2018 melting seasons identified as part of the temporal L-band signature analysis in this study (Section 2.3.1). As compared to ice slabs, which are dense low-permeability solid-ice layers, spatially coherent melt layers are a network of embedded ice structures primarily consisting of discontinuous horizontally-oriented ice layers and ice lenses sparsely connected via vertical-oriented ice pipes (Culberg et al., 2021). Spatially coherent melt layers are relatively thin (0.02 cm-2 m) and can rapidly form across the high-elevation (up to 3200 m a.s.l.) dry snow facies at depths of less than 1 m beneath the ice sheet surface following a single extreme melting season. They can further merge together into thicker solid-ice layers following multiple extreme melting seasons. Spatially coherent melt layers are exceptionally bright in AR radargrams (e.g., Fig 3a). The large dielectric contrast between the spatially coherent melt layer and the overlying, underlying, and interior snow and firn layers results in high reflectivity at the interfaces. However, electromagnetic energy still propagates downward through the high reflectivity layer into the deeper firn layers. Culberg et al., (2021) recently demonstrated mapping the extent of spatially coherent melt layers formed following the 2012 melting season (Nghiem et al., 2012) via AR (Figs. 1c; 2).

2.3 Empirical Algorithm

2.3.1 Temporal L-band Signatures over the Percolation Facies

T^B expresses the satellite-observed magnitude of thermal emission and is influenced by the microwave instrument's observation geometry as well as the depth- and time-integrated dielectric and geophysical properties of the ice sheet (Ulaby et al., 2014). The most significant geophysical property influencing T^B is the volumetric fraction of meltwater within the snow and firn pore space (Mätzler and Hüppi, 1989). During the melting season, the upper snow and firn layers of the percolation facies are saturated with large volumetric fractions of meltwater that percolates vertically into the deeper firn layers (Benson, 1960; Humphrey et al., 2012). Increases in the volumetric fraction of meltwater results in rapid relative increases in the imaginary part of the complex dielectric constant (Tiuiri et al., 1984). This typically increases T^B, and decreases volume scattering and penetration depth. The L-band penetration depth can rapidly decrease from tens to hundreds of meters to less than a meter, dependent on the local snow and firn conditions. During the freezing season, surface and subsurface water-saturated snow and firn layers and embedded ice structures subsequently refreeze. Decreases in the volumetric fraction of meltwater results in rapid

relative decreases in the imaginary part of the complex dielectric constant. This decreases T^B, and increases volume scattering and penetration depth. The L-band penetration depth increases back to tens to hundreds of meters on variable time scales.

We analyze melting and freezing seasons in temporal L-band signatures exhibited in T_V^B time series over and near the AR- and MCoRDS-derived perennial firn aquifer and ice slab detections projected on the NH EASE-Grid 2.0 (Fig. 4; Table 1). We project ice surface temperature observations calculated using thermal infrared brightness temperature collected by the Moderate Resolution Imaging Spectroradiometer (MODIS) on the Terra and Aqua satellites (Hall et al., 2012) on the NH EASE-Grid 2.0 at a 3.125 km rSIR grid cell spacing. We then derive melt onset and surface freeze-up dates for each rSIR grid cell using the methodology described in Miller et al., (2020). We set a threshold of ice surface temperature >−1°C for meltwater detection (Nghiem et al., 2012), consistent with the ±1°C accuracy of the ice surface temperature observations. For temperatures that are close to 0°C, ice surface temperatures are closely compatible with contemporaneous NOAA near-surface air temperature observations (Shuman et al., 2014). Melt onset and surface freeze-up dates are overlaid on T_V^B time series to partition the melting and freezing seasons. Melt onset dates typically occur between April and July, and surface freeze-up dates typically occur between July and September. The melting season increases in duration moving downslope from the dry snow facies, and ranges from a single day in the highest elevations (>2500 m) of the percolation facies, to 150 days in the ablation facies. Similarly, the freezing season decreases in duration moving downslope, and ranges from between 215 days and 365 days.

Over perennial firn aquifer areas (e.g., Fig. 4a, SMAP Test Site A: 66.2115°N, 39.1795°W, 1625 m a.s.l), maximum T_V^B ($T_{V,max}^B$) values are radiometrically warm during the melting season. Vertically percolating meltwater and gravity-driven meltwater drainage seasonally recharges perennial firn aquifers at depth (Fountain and Walder et al., 1998). Minimum T_V^B ($T_{V,min}^B$) values remain radiometrically warm during the freezing season as a result of latent heat continuously released by the slow refreezing of the deeper firn layers that are saturated with large volumetric fractions of meltwater (Miller et al, 2020). Temporal L-band signatures exhibit slow exponential decreases and approach, and sometimes achieve, stable T_V^B values. T_V^B can decrease by more than 50 K during the freezing season, which represents the descent of the upper surface of stored meltwater by meters to tens of meters (Miège et al., 2016).

Over ice slab areas (e.g., Fig. 4b, SMAP Test Site B: 66.8850°N, 42.7765°W, 1817 m a.s.l), $T_{V,max}^B$ values are typically radiometrically colder than over perennial firn aquifer areas during the melting season. The presence of dense low-permeability solid-ice layers reduces the snow and firn pore space available to store seasonal meltwater at depth. Meltwater may alternatively run-off ice slabs downslope towards the wet snow facies. $T_{V,min}^B$ values are also typically radiometrically colder than over perennial firn aquifer areas during the freezing season as a result of the absence of meltwater stored at depth. Temporal L-band signatures exhibit exponential decreases that are slightly more rapid than over perennial firn aquifer areas, and often achieve stable T_V^B values.

Over other percolation facies areas (e.g., Fig. 4c, SMAP Test Site C: 66.9024°N, 44.7528°W, 2350 m a.s.l), where seasonal meltwater is fully refrozen and stored exclusively as embedded ice, $T_{V,max}^{B}$ values are typically radiometrically colder than over perennial firn aquifer and ice slab areas during the melting season. $T_{V,min}^{B}$ values are also typically radiometrically cold during the freezing season. Temporal L-band signatures exhibit rapid exponential decreases, and achieve stable T_V^B values. However, over the highest elevations (>2500 m a.s.l.) of the percolation facies approaching the dry snow line, where seasonal surface melting and the formation of embedded ice structures is limited, $T_{V,min}^{B}$ values remain radiometrically warm during the freezing season. T_V^B decreases, often step-responses exceeding 10 K, are a result of an increase in volume scattering from newly formed embedded ice structures within a spatially coherent melt layer. Temporal L-band signatures that increase several K on time scales of years indicate the burial of spatially coherent melt layers formed following the 2010, 2012, 2015, and 2018 melting seasons by snow accumulation.

Exponentially decreasing temporal L-band signatures transition smoothly between perennial firn aquifer, ice slab, and other percolation facies areas – there are no distinct temporal L-band signatures that delineate boundaries between these sub-facies. Boundary transitions between the dry snow facies and the wet snow facies, however, are delineated above and below the percolation facies. Over the dry snow facies (e.g., Fig. 4d, SMAP Test Site D: 66.3649°N, 43.2115°W, 2497 m a.s.l), $T_{V,max}^{B}$ and $T_{V,min}^{B}$ values are radiometrically warm during the melting and freezing seasons. Temporal L-band signatures that increase on time scales of years are observed throughout the dry snow facies at elevations as high as Summit Station (3200 m a.s.l) and indicate the burial of the spatially coherent melt layer formed following the 2012 melting season (Nghiem et al., 2012) by snow accumulation (Culberg et al., 2021). Over the wet snow facies (e.g., Fig. 4e, SMAP Test Site E: 67.3454°N, 48.4789°W, 1469 m a.s.l), where seasonal meltwater is fully refrozen and stored as superimposed ice, $T_{V,max}^{B}$ values are radiometrically warm during the melting season. As compared to the percolation facies, where temporal L-band signatures exhibit rapid increases following melt onset, temporal L-band signatures reverse and exhibit rapid decreases. These reversals are a result of high reflectivity and attenuation at the fully water-saturated snow layer and/or at the wet rough superimposed ice-air interface. Meltwater runs-off superimposed ice downslope towards the ablation facies. $T_{V,min}^{B}$ values remain radiometrically warm during the freezing season. Temporal L-band signatures exhibit rapid increases, and achieve stable T_V^B values.

2.3.2 Two-Layer-L-band Brightness Temperature Model

Based on our analysis of $T_{V,max}^{B}$ and $T_{V,min}^{B}$ in temporal L-band signatures over the percolation facies (Section 2.3.1), we derive a 'firn saturation' parameter using a simple two-layer L-band brightness temperature model (Ashcraft and Long, 2006; Miller et al., 2021, in press). The 'firn saturation' parameter is similar to the 'melt intensity' parameter derived in Hicks and Long (2011) that uses enhanced resolution vertically-polarized Ku-band radar backscatter imagery (2003) collected by the SeaWinds radar scatterometer that was flown in tandem on NASA's Quick SCATterometer (QuikSCAT) satellite (Tsai et al.,

2000) and JAXA's Advanced Earth Observing Satellite 2 (ADEOS-II) (Freilich et al., 1994). We use the firn saturation parameter to estimate the maximum seasonal volumetric fraction of meltwater within the saturated upper snow and firn layers of the percolation facies using $T^B_{V,max}$ and $T^B_{V,min}$values extracted from T^B_V time series. We calculate the firn saturation parameter for each rSIR grid cell within the ice sheet-masked extent of the GrIS as part of our adapted empirical algorithm (Section 2.3.4).

We assume a base layer underlying a water-saturated firn layer with a given depth and volumetric fraction of meltwater. Each of the layers is homogenous. The ice sheet is discretely layered to calculate T^B_V at an oblique incidence angle (Eq. 1). Emission from the base layer is a function of both the macroscopic roughness and the dielectric properties of the layer. It occurs in conjunction with volume scattering at depth, and is locally dependent on embedded ice structures, spatially coherent melt layers, ice slabs, and perennial firn aquifers. Reflectivity at depth (i.e., at the base layer-water-saturated firn layer interface), and at the ice sheet surface (i.e., at the water-saturated firn layer-air interface) is neglected. The contribution from each layer is individually calculated.

The two-layer L-band brightness temperature model is represented analytically by

$$T^B_{V,max} = T\left(1 - e^{-\kappa_e d sec\theta}\right) + T^B_{V,min} e^{-\kappa_e d sec\theta}\ , \qquad \text{(Eq. 1)}$$

where $T^B_{V,max}$ is the maximum vertically-polarized L-band brightness temperature at the ice sheet surface, and represents emission from the maximum seasonal volumetric fraction of meltwater stored within the water-saturated firn layer. $T^B_{V,min}$ is the minimum vertically-polarized L-band brightness temperature emitted from the base layer. T is the physical temperature of the water-saturated firn layer, θ is the transmission angle, κ_e is the extinction coefficient, and d is depth.

We invert Eq. 1 and solve for the firn saturation parameter (ξ)

$$\xi = ln\left(\frac{T^B_{V,max} - T}{T^B_{V,min} - T}\right) cos\theta\ , \qquad \text{(Eq. 2)}$$

where $\xi = \kappa_e d$. The maximum vertically-polarized L-band brightness temperature asymptotically approaches the physical temperature of the water-saturated firn layer as the extinction coefficient and the depth of the water-saturated firn layer increases. For simplicity, we follow Jezek et al., (2015) and define the extinction coefficient as the sum of the Raleigh scattering coefficient (κ_s) and the absorption coefficient (κ_a). This assumes scattering from snow grains, which are small (millimeter scale) relative to the L-band wavelength (21 cm), and neglects Mie scattering from large (centimeter scale) embedded ice structures. However, for water-saturated firn, absorption dominates over scattering, and increases in the extinction coefficient are controlled by the volumetric fraction of meltwater (m_v).

We assume that thicker water-saturated firn layers with larger volumetric fractions of meltwater generate higher firn saturation parameter values. However, the thickness of the water-saturated firn layer is limited by the L-band penetration depth. Theoretical L-band penetration depths calculated for a water-saturated firn layer range from between 10 m for small volumetric fractions of meltwater (m_v<1%), and 1 cm for large volumetric fractions of meltwater (m_v=20%) (Fig. 5). Large volumetric fractions of meltwater

results in high reflectivity and attenuation at the water-saturated firn layer-air interface , and a radiometrically cold firn layer.

2.3.3 Continuous Logistic Model

We adapt our previously developed empirical algorithm to map the extent of Greenland's perennial firn aquifers (Miller et al., 2020) to also map the extent of ice slab areas. The empirical algorithm is derived from the continuous logistic model, which is based on a differential equation that models the decrease in physical systems as a function of time using a set of sigmoidal curves. These curves begin at a maximum value with an initial interval of decrease that is approximately exponential. Then, as the function approaches its minimum value, the decrease slows to approximately linear. Finally, as the function asymptotically reaches its minimum value, the decrease exponentially tails off and achieves stable values. We use the continuous logistic model to parametrize the refreezing rate within the water-saturated upper snow and firn layers of the percolation facies using T_V^B time series that are partitioned using $T_{V,max}^B$ and $T_{V,min}^B$ values. We calculate the refreezing rate for each rSIR grid cell within the percolation facies extent as part of our adapted empirical algorithm (Section 2.3.4).

The continuous logistic model is described by a differential equation known as the logistic equation

$$\frac{dx}{dt} = \zeta x(1-x) \quad \text{(Eq. 3)}$$

that has the solution

$$x(t) = \frac{1}{1+\left(\frac{1}{x_o}-1\right)e^{-\zeta t}}, \quad \text{(Eq. 4)}$$

where x_o is the function's initial value, ζ is the function's exponential rate of decrease, and t is time. The function $x(t)$ is also known as the sigmoid function. We use the sigmoid function to model the exponentially decreasing temporal L-band signatures observed over the percolation facies as a set of decreasing sigmoidal curves.

We first normalize T_V^B time series for each rSIR grid cell

$$T_{V,N}^B(t) = \frac{T_V^B(t)-T_{V,min}^B}{T_{V,max}^B-T_{V,min}^B}, \quad \text{(Eq. 5)}$$

where $T_{V,min}^B$ is the minimum vertically-polarized L-band brightness temperature, and $T_{V,max}^B$ is the maximum vertically-polarized L-band brightness temperature. We then apply the sigmoid fit

$$T_{V,N}^B\left(t \in [t_{max}, t_{min}]\right) = \frac{1}{1+\left(\frac{1}{T_{V,N}^B(t_{max})}-1\right)e^{-\zeta t}}. \quad \text{(Eq. 6)}$$

$T_{V,N}^B\left(t \in [t_{max}, t_{min}]\right)$ is the normalized vertically-polarized L-band brightness temperature on the time interval $t \in [t_{max}, t_{min}]$, where t_{max} is the time the function achieves a maximum value, and t_{min} is the time the function achieves a minimum value. The initial normalized vertically-polarized L-band brightness temperature ($T_{V,N}^B(t_{max})$) is the function's maximum value. The final normalized vertically-polarized L-band

brightness temperature ($T_{V,N}^{B}(t_{min})$) is the function's minimum value. The function's exponential rate of decrease represents the refreezing rate parameter (ζ). An example set of simulated sigmoidal curves is shown in Fig. 6.

2.3.4 SMAP-Derived Perennial Firn Aquifer and Ice Slab Mapping

Our adapted empirical algorithm is implemented in two steps: (1) mapping the extent of the percolation facies using the firn saturation parameter derived from the simple two-layer L-band brightness temperature model (Section 2.3.2), and (2) mapping the extent of perennial firn aquifer and ice slab areas over the percolation facies using the continuous logistic model (Section 2.3.3) we calibrate using airborne ice-penetrating radar surveys (Section 2.2).

Using Eq. 2, we first set a threshold for the firn saturation parameter (ξ_T) defined by the relationship

$$\xi_T = (\kappa_s + \kappa_a)d \leq \xi \ . \quad \text{(Eq. 7)}$$

We calculate the Raleigh scattering coefficient (κ_s) in Eq. 7 using

$$\kappa_s = N_d \frac{8}{3} k_o^4 r^6 \left|\frac{\varepsilon_r - 1}{\varepsilon_r + 2}\right|^2 , \quad \text{(Eq. 8)}$$

where N_d is the particle density, k_o is the wave number of the background medium of air, r is the snow grain radius set to r=2 mm, and ε_r is the complex dielectric constant. The particle density is defined by

$$N_d = \frac{\rho_{firn}}{\rho_{ice}} \frac{1}{\frac{4}{3}\pi r^3} , \quad \text{(Eq. 9)}$$

where ρ_{firn} is firn density set to ρ_{firn}=400 kg/m^3, and ρ_{ice} is ice density set to ρ_{ice}=917 kg/m^3. Our grain radius and firn density estimates are consistent with measurements within the upper snow and firn layers of the percolation facies of south eastern Greenland at the Helheim Glacier field site (Fig. 2a, blue circle), where in situ perennial firn aquifer measurements have recently been collected (Miller et al., 2017).

We calculate the absorption coefficient (κ_a) in Eq. 7 using

$$\kappa_a = -2k_o \Im\{\sqrt{\varepsilon_r}\} , \quad \text{(Eq. 10)}$$

where $\Im\{\}$ represents the imaginary part. We calculate the complex dielectric constant of the water-saturated firn layer in Eq. 8 and Eq. 10 using the empirically derived models described in Tiuri et al., (1984). We set the volumetric fraction of meltwater to m_v=1%. We set the depth of the water-saturated firn layer in Eq. 7 to d=1 m. These values are consistent with typical lower frequency (e.g., 37 GHz, 13.4 GHz, 19 GHz) passive (e.g., Mote, et al. 1995; Abdalati and Steffen, 1997; Ashcraft and Long, 2006) and active (e.g., Hicks and Long, 2011) microwave algorithms used to detect seasonal surface melting over the GrIS. Using the results of Eq. 7, 8, 9, and 10, we calculate the firn saturation parameter threshold at ξ_T=0.1.

The first step in our adapted empirical algorithm is to map the extent of the percolation facies. For each rSIR grid cell within the ice sheet-masked extent of the GrIS, we smooth the corresponding T_V^B time series using a 14-observation (1 week) moving window. We extract the minimum vertically-polarized L-band brightness temperature ($T_{V,min}^{B}$), and the maximum vertically-polarized L-band brightness temperature

($T^B_{V,max}$). We set the physical temperature of the water-saturated firn layer to T=273.15 K, and the transmission angle to θ=40°. We then calculate the firn saturation parameter (ξ) using Eq. 2. If the calculated firn saturation parameter exceeds the firn saturation parameter threshold, the rSIR grid cell is converted to a binary parameter to map the total extent of the percolation facies.

We note that smoothing T^B_V time series will mask brief low-intensity seasonal surface melting that occurs in the high-elevation (>2500 m) percolation facies, where seasonal meltwater is rapidly refrozen within the colder snow and firn layers (e.g., Fig. 4d). Thus, the calculated firn saturated parameter will not exceed the firn saturation parameter threshold, and these rSIR grid cells will be excluded from the algorithm. The exclusion of rSIR grid cells in the high-elevation percolation facies is not expected to have a significant impact on our results as our algorithm targets rSIR grid cells in areas that experience intense seasonal surface melting. The exclusion of rSIR grid cells will, however, slightly underestimate the mapped percolation facies extent.

The second step in our adapted empirical algorithm is to map the extent of perennial firn aquifer and ice slab areas over the percolation facies. For each rSIR grid cell within the mapped percolation facies extent, we normalize the corresponding T^B_V time series ($T^B_{V,N}(t)$) using Eq. 5. We then extract the initial normalized vertically-polarized L-band brightness temperature ($T^B_{V,N}(t_{max})$) and the final normalized vertically-polarized L-band brightness temperature ($T^B_{V,N}(t_{min})$), and partition $T^B_{V,N}(t)$ on the time interval $t \in [t_{max}, t_{min}]$. We smooth $T^B_{V,N}(t \in [t_{max}, t_{min}])$ using a 56-observation (4 week) moving window. The sigmoid fit is then iteratively applied using Eq. 6. Smoothing reduces the chi-squared error statistic when fitting $T^B_{V,N}(t \in [t_{max}, t_{min}])$ to the sigmoid function. We fix the initial normalized vertically-polarized L-band brightness temperature at $T^B_{V,N}(t_{max})$=0.99, which provides a uniform parameter space in which the refreezing rate parameter (ζ) can be analyzed. Variability in $T^B_{V,N}(t_{max})$ is controlled by the volumetric fraction of meltwater within the upper snow and firn layers of the percolation facies, and is accounted for in the firn saturation parameter (ξ), which is analyzed separately. $T^B_{V,N}(t \in [t_{max}, t_{min}])$ iteratively fit to the sigmoid function converge quickly (i.e., algorithm iterations $I \in [5, 15]$), and observations are a good fit (i.e., chi squared error statistic is $\chi 2 \in [0, 0.1]$).

Using the SMAP-derived $T^B_{V,N}(t_{max})$ and $T^B_{V,N}(t_{min})$, rather than the MODIS-derived initial normalized vertically-polarized L-band brightness temperature at the surface freeze-up date ($T^B_{V,N}(t_{sfu})$), and final normalized vertically-polarized L-band brightness temperature at the melt onset date ($T^B_{V,N}(t_{mo})$) that were used in the empirical algorithm described in Miller et al., 2020 has several advantages. They key advantage of this approach is that maps can be generated using T^B imagery collected from a single satellite, which simplifies our adapted empirical algorithm. Another advantage is that unlike T^B collected at shorter-wavelength thermal infrared frequencies (e.g., MODIS), T^B collected at longer wavelength microwave frequencies (e.g., SMAP) is not sensitive to clouds, which eliminates observational gaps and cloud contamination, and provides more accurate time series partitioning and more robust curve fitting.

We calibrate our adapted empirical algorithm using the AR- and MCoRDS-derived perennial firn aquifer and ice slab detections projected on the NH EASE-Grid 2.0. For each rSIR grid cell with at least one detection, we extract the correlated maximum vertically-polarized L-band brightness temperature ($T^B_{V,max}$), the minimum vertically-polarized L-band brightness temperature ($T^B_{V,min}$), the firn saturation parameter (ξ), and the refreezing rate parameter (ζ). For each of the extracted calibration parameters, we calculate the standard deviation (σ). Thresholds of $\pm 2\sigma$ are set in an attempt to eliminate peripheral rSIR grid cells near the ice sheet edge and near the boundaries of each sub-facie, where L-band emission can be influenced by morphological features, such as crevasses, superimposed and glacial ice, and spatially integrated with emission from rock, land, the ocean, and adjacent percolation facies and wet snow facies areas. The calibration parameter intervals are given in Table 2**.** We apply the calibration to each rSIR grid cell within the percolation facies extent. If the extracted calibration parameters are within the intervals, the rSIR grid cell is converted to a binary parameter to map the total extent of each of these sub-facies.

Miller et al., 2020 cited significant uncertainty in the SMAP-derived perennial firn aquifer extent as a result of the lack of a distinct temporal L-band signature delineating the boundary between perennial firn aquifer areas and adjacent percolation facies areas. In this study, similar uncertainty exists in the SMAP-derived perennial firn aquifer and ice slab extents. This uncertainty could, at least in part, be a result of the rSIR algorithm. An rSIR grid cell corresponds to the weighted average of T^B over SMAP's antenna footprint (Long et al., 2020). The weighting is the grid cell's spatial response function (SRF), which is approximately 18 km (i.e., the effective resolution) in diameter. The SRF is centered on the rSIR grid cell. Since the effective resolution (i.e., the size of the 3 dB contour of the SRF) is less than the rSIR grid cell spacing, rSIR grid cell SRF's overlap and the grid cells T^B values are not statistically independent. This uncertainty, however, could also have a geophysical basis, as it is unlikely that the boundaries between sub-facies as well as between facies are distinct. The thickness of the water-saturated firn layer or ice slab may thin and taper-off at the periphery, and sub-facies and facies may become spatially scattered and merge together.

The limited extent (AR, 15 m x 20 m; MCoRDS, 14 m x 40 m) of the airborne ice-penetrating radar surveys as compared to the rSIR grid cell extent (3.125 km) and the effective resolution of the SMAP enhanced-resolution T^B_V imagery is also cited in Miller et al., 2020 as a source of uncertainty in the empirical algorithm. In this study, similar uncertainty exists in our adapted empirical algorithm. The total rSIR grid cell extent with airborne ice-penetrating radar survey coverage is less than 2%. Thus, 98% of the total rSIR grid cell extent from which the SMAP-derived calibration parameter intervals are extracted is unknown. Calculating the total rSIR grid cell extent where detections are absent along OIB flight lines and statistically integrating this calculation into the multi-year calibration technique may help reduce the uncertainty, particularly the significant uncertainty in the interannual variability in extent, which we have yet to resolve. A sensitivity analysis suggests that even small changes in the SMAP-derived calibration parameter intervals (i.e., several K for $T^B_{V,min}$, and $T^B_{V,max}$, several tenths of a percentage point for ξ, and several hundredths of a percentage point for ζ) can result in variability in the mapped extents of hundreds of square kilometers, and boundary transitions between perennial firn aquifer and ice slab areas. Thus, the mapped extent of

each of these sub-facies should simply be considered an initial result demonstrating the potential of our adapted empirical algorithm for future work.

3. Results and Discussion

The SMAP-derived maximum vertically-polarized L-band brightness temperature values generated by our adapted empirical algorithm range from between $T^B_{V,max}$=150 K and 275 K, and the minimum vertically-polarized L-band brightness temperature values range from between $T^B_{V,min}$=130 K and 250 K. These values are consistent with the range of $T^B_{V,max}$ and $T^B_{V,min}$ values given in the temporal L-band signature analysis (Table 1). Firn saturation parameter values range from between ξ=0.1 and 4.0. Refreezing rate parameter values range from between ζ=-0.09 and -0.01. The observed lower bound (ζ=-0.09) of the refreezing rate parameter is significantly higher than the predicted lower bound (ζ=-1) in our example set of simulated sigmoidal curves (black line, Fig. 6).

The SMAP-derived perennial firn aquifer, ice slab, and percolation facies extents are shown in Figs. 7a-9a. The percolation facies extent (5.8 x 10^5 km^2) is mapped at elevations between 500 m a.s.l. and 3500 m a.s.l., and extends over 32 % of the GrIS extent (1.8 x 10^6 km^2). The perennial firn aquifer extent (64,000 km^2) is mapped at elevations between 600 m a.s.l and 2600 m a.s.l., and extends over 11% of the percolation facies extent, and 4% of the GrIS extent. Predominately high $T^B_{V,max}$, $T^B_{V,min}$, ξ, and ζ values mapped within the perennial firn aquifer extent indicates the widespread presence of thicker water-saturated firn layers with larger volumetric fractions of meltwater that are radiometrically warm during both the melting and freezing seasons, and have extended refreezing rates. The ice slab extent (76,000 km^2) is mapped at elevations between 800 m a.s.l and 2700 m a.s.l., and extends over 13 % of the percolation facies extent, and 4 % of the GrIS extent. As compared to perennial firn aquifer areas, decreased $T^B_{V,max}$, $T^B_{V,min}$, ξ and ζ values in ice slabs areas indicates the presence of thinner water-saturated firn layers with lower volumetric fractions of meltwater that are radiometrically colder, and have slightly more rapid refreezing rates. Combined together, the total extent (140,000 km^2) is the equivalent of 24% of the percolation facies extent, and 10% of the GrIS extent. The extents of these sub-facies are generally isolated and somewhat scattered within the percolation facies. However, in several areas in south, south and central eastern, and northern Greenland, the sequential formation of facies and sub-facies (dry snow facies - percolation facies - ice slab - perennial firn aquifer – ablation facies) is mapped.

Figs. 7b-9b shows perennial firn aquifers, ice slabs, and spatially coherent melt layers detected by airborne ice-penetrating radar surveys overlaid on the SMAP-derived percolation facies extent**.** The SMAP-derived perennial firn aquifer extent mapped in southern, and south and central eastern Greenland is consistent with the AR- and MCoRDS-derived perennial firn aquifer detections. Additional smaller perennial firn aquifer areas are mapped in northern Greenland. The SMAP-derived ice slab extent mapped in south western, and central eastern Greenland is generally consistent with the spatial patterns of the AR-derived ice slab detections, however, is significantly expanded upslope in each of these areas. In northern

Greenland, perennial firn aquifers areas are alternatively mapped, and additional expansive ice slab areas are mapped upslope of perennial firn aquifer areas. Additional smaller ice slab areas are mapped in south and south eastern Greenland. We note that the AR- and MCoRDS-derived perennial firn aquifer and ice slab detections are limited in space and time, particularly in northern Greenland, with a time interval as large as nine years between the airborne ice-penetrating radar surveys and the SMAP enhanced-resolution T_V^B imagery we use in our adapted empirical algorithm. In western and northern Greenland, the 2015 melting season was especially intense (Tedesco et al., 2016). And, in northern Greenland, the ablation facies have recently (2010-2019) increased in extent (Noël et al., 2019), and supraglacial lakes have recently (2014-2019) advanced inland (Turton et al., 2021), indicating a possible geophysical basis for the observed formation, boundary transitions, and expansion. Neither perennial firn aquifer or ice slab areas are mapped on the Maniitsoq and Flade Isblink Ice Caps, where spatially integrated L-band emission results in calibration parameter values outside the defined intervals for each of these sub-facies.

Although the AR-derived spatially coherent melt layers detections are often observed to be adjacent to perennial firn aquifer and ice slab areas, these sub-facies were masked in the original airborne ice penetrating radar survey analysis by Culberg et al., (2021). Spatially coherent melt layers often overlay perennial firn aquifers (e.g., Fig. 3a), and merge with ice slabs (Culberg et al., 2021; Fig.4).

Shallow buried supraglacial lakes have recently been identified within the percolation facies of western, northern, and north and central eastern Greenland using airborne ice-penetrating radar surveys (Koenig et al., 2015) and satellite synthetic aperture radar imagery (Miles et al., 2017; Schröder et al., 2020; Dunmire et al., 2021). These buried supraglacial lakes are within the SMAP-derived perennial firn aquifer and ice slab extents, however, are not expected to significantly influence L-band emission in these areas for two reasons. (1) As compared to SMAP's 18 km footprint, the mean extent of buried supraglacial lakes is limited (less than 1 km^2), and they are sparsely distributed in perennial firn aquifer and ice slab areas (Dunmire et al., 2021). (2) Supraglacial lakes form during the melting season as a result of meltwater storage within topographic depressions at the ice sheet surface (Echelmeyer et al. 1991). Similar to subglacial lakes (Jezek et al., 2015) and perennial firn aquifers (Miller et al., 2020), supraglacial lakes represent radiometrically cold near-surface meltwater reservoirs. Upwelling L-band emission from deeper firn layers, superimposed and/or glacial ice, and the underlying bedrock are effectively blocked by high reflectivity and attenuation at the interface between the lake bottom and the underlying impermeable layer. This results in low observed T^B at the upper surface of meltwater stored within supraglacial lakes. During the freezing season, the upper surface of meltwater refreezes and forms a partial or solid-ice cap that is sometimes buried by snow accumulation (Koenig et al., 2015). Airborne ice-penetrating radar surveys in April and May between 2009 and 2012 suggest the mean depth to the upper surface of meltwater stored within buried supraglacial lakes is approximately 2 m (Koenig et al., 2015). Over buried supraglacial lakes, L-band emission from the refreezing partial or solid-ice cap, which is smooth relative to the L-band wavelength (21 cm), likely induces surface scattering. As a result, T_V^B decreases over buried supraglacial

lakes are likely negligible. Thus, over SMAP's 18 km footprint, we postulate water-saturated firn layers dominate L-band emission over the percolation facies of the GrIS.

The SMAP-derived perennial firn aquifer extent (64,000 km^2) generated by our adapted empirical algorithm and the multi-year calibration technique (2015-2019) is consistent with the extent (66,000 km^2) generated by the previously developed empirical algorithm and the single-coincident year calibration technique (2016) described in Miller et al., 2020. The SMAP-derived perennial firn aquifer extent is generally consistent with previous C-band (5.3 GHz) satellite radar scatterometer-derived perennial firn aquifer extents mapped using the Advanced SCATterometer (ASCAT) on the European Organization for the Exploitation of Meteorological Satellites (EUMETSAT) Meteorological Operational A (MetOp-A) satellite (2009-2016, 52 000-153 000 km^2; Miller, 2019), and the Active Microwave Instrument in radar scatterometer mode (ESCAT) on ESA's European Remote Sensing (ERS) satellite series (1992-2001, 37 000-64 000 km^2; Miller, 2019) as well as the C-band (5.4 GHz) synthetic aperture radar-derived extent mapped using ESA's Sentinel-1 satellite (2014-2019, 54 000 km^2; Brangers et al., 2020). The exception is the ASCAT-derived perennial firn aquifer extent (2012-2013, 153,000 km^2; Miller, 2019) mapped following the 2012 melting season (Nghiem et al., 2012) in which significant changes in the dielectric and geophysical properties that influence radar backscatter likely occurred. The unreasonably expansive (i.e., more than twice the mean) mapped extent is a result of ASCAT'S shallow (several meters) C-band penetration depth (Jezek et al., 1994), and the simple threshold-based algorithm, which was not calibrated for an extreme melting season that included saturation of the upper snow and firn layers of the dry snow facies and percolation facies with relatively large volumetric fractions of meltwater (Miller et al., 2019). Water-saturated firn layers had extended refreezing rates, however, seasonal meltwater was not stored at depth. Widespread spatially coherent melt layers were alternatively formed in many of the mapped areas (Culberg et al., 2021). The SMAP-derived ice slab extent (76,000 km^2) is also consistent with previous AR-derived ice slab extents (2010-2014, 64,800 km^2-69,400 km^2; McFerrin et al., 2019).

Although we simply consider our mapped extents a high-probability area for preferential formation, the maps generated by our adapted empirical algorithm and the multi-year calibration technique for individual years suggest there reasonable interannual variability in perennial firn aquifer and ice and slab extents (Table 3). Our results demonstrate sensitivity to the variability in the depth- and time-integrated dielectric and geophysical properties of the percolation facies that influence the radiometric temperature, even during the 2015 melting season (Tedesco et al., 2016).

4 Implications

Seasonal surface melting over the GrIS has increased in extent, intensity, and duration since early in the satellite era (Steffen et al., 2004; Tedesco e al., 2008; Tedesco et al., 2011; Nghiem et al., 2012; Tedesco et al., 2016; Tedesco and Fettweis, 2020; Cullather et al., 2020). Consistent with recent seasonal surface melting trends, meltwater run-off has accelerated to become the dominant mass loss mechanism over the GrIS (van den Broeke et al., 2016). Meltwater storage in both solid (i.e., embedded ice structures, including ice slabs, spatially coherent melt layers) and liquid (i.e., perennial firn aquifers) form can buffer meltwater

run-off in the percolation facies and delay its eventual release into the ocean (Harper et al., 2012). However, significant uncertainty remains in meltwater run-off estimates as a result of the lack of knowledge of heterogeneous infiltration and refreezing processes within the snow and firn layers (Pfeffer and Humphrey, 1996), and the depths to which meltwater can descend beneath the ice sheet surface (Humphrey et al., 2012).

If the increasing seasonal surface melting trend continues (Franco et al., 2013; Noël et al., 2021), perennial firn aquifer formation and expansion may increase the possibility of crevasse-deepening via meltwater-induced hydrofracturing (Alley et al., 2005; van der Veen, 2007), especially if crevasse fields expand into perennial firn aquifer areas as a result of accelerated ice flow (Colgan et al., 2016). Meltwater-induced hydrofracturing is an important component of supraglacial lake drainage during the melting season (Das et al., 2008; Stevens et al., 2015) leading to at least temporary localized accelerated ice flow velocities (Zwally et al., 2002; Joughin et al., 2013; Moon et al., 2014) as well as ice discharge from outlet glaciers (Chudley et al., 2019), and mass balance changes (Joughin et al., 2008). Perennial firn aquifers may also support meltwater-induced hydrofracturing, even during the freezing season (Poinar et al., 2017; Poinar et al., 2019).

The formation and expansion of ice slabs reduces permeability within the upper snow and firn layers and facilitates lateral meltwater flow with minimum vertical percolation into the deeper firn layers, thereby enhancing meltwater run-off and mass loss at the periphery (MacFerrin et al., 2019). Lateral meltwater flow across ice layers overlying deeper permeable firn layers was first postulated by Müller (1962). The theory was then further developed by Pfeffer et al., (1991) as an end-member case for meltwater run-off in the percolation facies, with the other end member case being lateral meltwater flow across superimposed ice in the wet snow facies and/or across glacial ice in the ablation facies. Lateral meltwater flow and high-elevation (1850 m a.s.l) meltwater run-off across ice slabs in the percolation facies was recently observed in visible satellite imagery collected by the NASA-USGS Landsat 7 mission during the 2012 melting season (MacFerrin et al., 2019).

Spatially coherent melt layers represent a newly identified end-member case for meltwater runoff in the dry snow facies (Culberg et al., 2021). Similar to ice slabs, the formation and expansion of spatially coherent melt layers reduces the pore space within the upper snow and firn layers, and may also facilitate lateral meltwater flow with minimum vertical percolation into the deeper firn layers, thereby enhancing meltwater run-off from significantly higher elevations on accelerated time scales. The rapid formation of spatially coherent melt layers that merge with ice slabs upslope of perennial firn aquifers areas may simultaneously accelerate both meltwater run-off and meltwater-induced hydrofracturing during extreme melting seasons. The formation of spatially coherent melt layers overlying deeper perennial firn aquifers may result in the formation of shallow perched firn aquifers (Culberg et al., 2021), or may terminate gravity-driven meltwater drainage and seasonal recharging (Fountain and Walder, 1998), which may eventually completely refreeze stored meltwater into ice slabs or decimeters thick solid-ice layers overlying deeper glacial ice.

5 Summary and Future Work

In this study, for the first time, we have demonstrated the novel use of the L-band microwave radiometer on NASA's SMAP satellite for mapping perennial firn aquifers and ice slabs together as a continuous system over the percolation facies of the GrIS. We have adapted our previously developed empirical algorithm (Miller et al., 2020) by expanding our analysis of spatiotemporal differences in SMAP enhanced-resolution T_V^B imagery and temporal L-band signatures. We have used this analysis to derive a firn saturation parameter from a simple two-layer L-band brightness temperature model (Miller et al., 2021, in press). And, we have used the firn saturation parameter to map the extent of the percolation facies. We have found that by correlating maximum and minimum T_V^B values, the firn saturation parameter, and the refreezing rate parameter with perennial firn aquifer and ice slab detections identified via the CReSIS AR and MCoRDS instruments flown by NASA's OIB campaigns that we can calibrate our previously developed empirical algorithm (Miller et al., 2020) to map plausible extents.

We note that significant uncertainty exists in the mapped extents as a result of: (1) correlating the SMAP-derived parameters with airborne ice-penetrating radar detections that are not coincident in time, (2) the lack of a distinct temporal L-band signature delineating the boundary between perennial firn aquifer areas, ice slabs areas, and adjacent percolation facies areas, and (3) the limited extent of the airborne ice-penetrating radar detections as compared to the rSIR grid cell extent and the effective resolution of the SMAP enhanced-resolution T_V^B imagery.

Miller et al., (2020) normalized SMAP enhanced-resolution T_V^B time series and converted the exponential rate of T_V^B decrease over perennial firn aquifer areas to a binary parameter to map extent. In this study, we have converted the SMAP-derived parameters to binary parameters to map the extent of both perennial firn aquifer and ice slab areas. Moreover, we have included additional analysis of the spatiotemporal differences in maximum and minimum T_V^B values, the firn saturation parameter, and the refreezing rate parameter. We have shown that spatiotemporal differences in the SMAP-derived parameters are consistent with our assumption of spatiotemporal differences in the englacial hydrology and thermal characteristics of firn layers at depth.

Future work will focus on simulating temporal L-band signatures observed over perennial firn aquifer and ice slab areas for a wide range of geophysical properties. To better interannual variability in extent, we will interpret our results together with climatological parameters, such as snow accumulation, liquid water content, and surface mass balance simulated by the Regional Atmospheric Climate Model (RACMO2.3p2; Noël et al., 2018). Additionally, we will simulate the distinct temporal L-band signatures observed over spatially coherent melt layers and explore mapping the extent.

Combining multi-layer depth-integrated L-band brightness temperature models (e.g., Jezek et al., 2015) that include embedded ice structure parametrizations (e.g., Jezek et al., 2018) with models of depth-dependent geophysical parameters can lead to an improved understanding of the extremely complex and poorly described physics controlling L-band emission over the percolation facies. Key geophysical parameters include atmospheric temperature forcing, physical temperature versus depth, latent heat, snow

accumulation, the volumetric fraction and depth of meltwater, and the volumetric fraction and geometric configuration of embedded ice structures. The development of more sophisticated empirical algorithms that incorporate multi-layer depth-integrated L-band brightness temperature models that are constrained by in situ measurements can help reduce the significant uncertainty in the current mapped extents, and provide more accurate boundary delineation that can be used to further quantify the interannual variability in future mapped extents of perennial firn aquifer, ice slabs and spatially coherent melt layer areas.

Data Availability

SMAP Radiometer Twice-Daily rSIR-Enhanced EASE-Grid 2.0 Brightness Temperatures, Version 1 (2015-2019) have been produced as part of the NASA Science Utilization of SMAP project and are available at https://doi.org/10.5067/QZ3WJNOUZLFK (Brodzik et al., 2019). The NASA MEaSUREs Greenland Ice Mapping Project (GIMP) Land Ice and Ocean Classification Mask, Version 1, is available at https://doi.org/10.5067/B8X58MQBFUPA (Howat, 2017), and the Digital Elevation Model, Version 1, is available at https://nsidc.org/data/nsidc-0645/versions/1 (Howat et al., 2015). The coastline data are available from GSHHG – A Global Self-consistent, Hierarchical, High-resolution Geography Database https://doi.org/10.1029/96JB00104 (Wessel and Smith, 1996). Ice surface temperature imagery (2015-2019) have been produced as part of the Multilayer Greenland Ice Surface Temperature, Surface Albedo, and Water Vapor from MODIS V001 data set and are available at https://doi.org/10.5067/7THUWT9NMPDK (Hall and DiGirolamo, 2019). OIB AR- and MCoRDS-derived perennial firn aquifers detections (2010-2017) are available at https://arcticdata.io/catalog/view/doi:10.18739/A2985M (Miège et al., 2016). OIB AR-derived ice slab detections (2010-2014) are available at https://doi.org/10.6084/m9.figshare.8309777 (MacFerrin et al., 2019). OIB AR-derived spatially coherent melt layer detections (2017) are available at (https://doi.org/10.18739/A2736M33W) (Culberg et al., 2021). OIB AR L1B Geolocated Radar Echo Strength Profiles, Version 2, are available at, https://doi.org/10.5067/0ZY1XYHNIQNY (Paden et al., 2018). NASA MEaSUREs MODIS Mosaic of Greenland (MOG) 2015 Image Map, Version 2, is available at https://nsidc.org/data/NSIDC-0547/versions/2 (Haran et al., 2018). SMAP-derived perennial firn aquifer, ice slab, and perched firn aquifer extents are available from JZM upon request.

Author Contributions

JZM initiated the study, adapted the empirical model, performed the analyses, and wrote the manuscript. RC processed and interpreted the OIB AR radargram profiles. RC and DMS provided the spatially coherent melt layer detections. All authors participated in discussions and reviewed manuscript drafts.

Competing Interests

The authors declare that they have no conflict of interest.

Financial Support

JZM, DGL, and MJB are supported by the NASA SMAP Science Team (no. 80NSSC20K1806), and by the NASA Cryospheric Science Program (no. 80NSSC18K1055 and no. 80NSSC21K0749) under grants to the University of Colorado and Brigham Young University. RC is supported by a National Defense Science and Engineering Graduate Fellowship. RC and DMS are supported in part by NASA (no. NNX16AJ95G and NSF (no. 1745137). CAS is supported by the NASA Headquarters Cryospheric Science Program. We acknowledge the use of data from CReSIS generated with support from the University of Kansas, NASA Operation IceBridge grant NNX16AH54G, NSF grants ACI-1443054, OPP-1739003, and IIS-1838230, Lilly Endowment Incorporated, and Indiana METACyt Initiative.

References

Abdalati, W., and Steffen, K.: Snowmelt on the Greenland Ice Sheet as derived from passive microwave satellite data, J. Climate, 10, 165-175, https://doi.org/10.1175/1520-0442(1997)010<0165:SOTGIS>2.0.CO;2, 1997.

Alley, R. B., Dupont, T. K., Parizek, B. R., Anandakrishnan, S.: Access of surface meltwater to beds of sub-freezing glaciers: Preliminary insights, Ann. Glaciol., 40, 8-14, https://doi.org/10.3189/172756405781813483, 2005.

Ashcraft, I. and Long, D.: Comparison of methods for melt detection over Greenland using active and passive microwave measurements, Int. J. Remote Sens., 27, 2469-2488, https://doi.org/10.1080/01431160500534465, 2006.

Benson, C. S.: Stratigraphic studies in the snow and firn of the Greenland Ice Sheet, Ph.D. thesis, California Institute of Technology, 228 pp., 1960.

Bindschadler, R. A., Jezek, K. C., and Crawford, J.: Glaciological investigations using the synthetic aperture radar imaging system, Ann. Glaciol., 9, 11-19. https://doi.org/10.1017/S0260305500200694, 1987.

Brangers, I., Lievens, H., Miège, C., Demuzere, M., Brucker, L., and De Lannoy, G. J. M.: Sentinel-1 detects firn aquifers in the Greenland Ice Sheet, Geophys. Res. Lett., 47, e2019GL085192, https://doi.org/10.1029/2019GL085192, 2020.

Brodzik, M. J., Long, D. G., and Hardman, M. A.: SMAP Radiometer Twice-Daily rSIR-Enhanced EASE-Grid 2.0 Brightness Temperatures, Version 1, NASA National Snow and Ice Data Center Distributed Active Archive Center,https://doi.org/10.5067/QZ3WJNOUZLFK, 2019.

Brodzik, M. J., Billingsley, B., Haran, T., Raup, B., and Savoie, M. H.: EASE-Grid 2.0: Incremental but significant improvements for Earth-gridded data sets, ISPRS Int. J. Geo-Inf., 1, 32-45, https://doi.org/10.3390/ijgi1010032, 2012.

Chu, W., Schroeder, D. M., and Siegfried, M. R.: Retrieval of englacial firn aquifer thickness from ice-penetrating radar sounding in southeastern Greenland, Geophys. Res. Lett., 45, 11,770-11,778, https://doi.org/10.1029/2018GL079751, 2018.

CReSIS: CReSIS radar depth sounder data, Digital Media, http://data.cresis.ku.edu/, 2016.

Colgan, W., Rajaram, H., Abdalati, W., McCutchan, C., Mottram, R., Moussavi, M. S., and Grigsby, S.: Observations, models, and mass balance implications: Glacier crevasses, Rev. Geophys., 54, 119-161, https://doi.org/10.1002/2015RG000504, 2016.

Culberg, R., Schroeder, D.M. and Chu, W.: Extreme melt season ice layers reduce firn permeability across Greenland, Nat Commun, **12,** 2336, https://doi.org/10.1038/s41467-021-22656-5, 2021

Culberg, R.: Refrozen melt layer location, density, and connectivity records from airborne radar sounding, Greenland, NSF Arctic Data Center, https://doi.org/10.18739/A2736M33W, 2021.

Cullather, R. I., Andrews, L. C., Croteau, M. J., Digirolamo, N. E., Hall, D. K., Lim, Y., Loomis, B. D., Shuman, C. A., and Nowicki, S. M. J.: Anomalous circulation in July 2019 resulting in mass loss on the Greenland Ice Sheet. Geophys. Res. Lett., 47, https://doi.org/10.1029/2020GL087263, 2020.

Das, S. B., Joughin, I., Behn, M. D., Howat, I. M., King, M. A., Lizarralde, D., Bhatia, M. P., Fracture propagation to the base of the Greenland Ice Sheet during supraglacial lake drainage, Science, 320, 778-781, https://doi.org/10.1126/science.1153360, 2008.

Drinkwater, M. R., Long, D. G., and Bingham, A. W.: Greenland snow accumulation estimates from satellite radar scatterometer data, J. Geophys. Res. Atmos., 106, 33935-33950. https://doi.org/10.1029/2001JD900107, 2001.

Dunmire, D., Banwell, A. F., Lenaerts, J. T. M., and Datta, R. T.: Contrasting regional variability of buried meltwater extent over two years across the Greenland Ice Sheet, The Cryosphere Discuss, https://doi.org/10.5194/tc-2021-3, in review, 2021.

Early, D. S., and Long, D. G.: Image reconstruction and enhanced-resolution imaging from irregular samples, IEEE Trans. Geosci. Remote Sens. 39, 291-302, https://doi.org/10.1109/36.905237, 2001.

Echelmeyer, K., Clarke, T. S., and Harrison, W. D.: Surficial glaciology of Jakobshavn Isbræ, West Greenland 1. Surface morphology, J. Glaciol., 37, 368–382, https://doi.org/10.1017/S0022143000005803, 1991.

Entekhabi, D., et al.: The Soil Moisture Active Passive (SMAP) Mission, Proc. IEEE, 98, 704-716, https://doi.org/10.1109/JPROC.2010.2043918, 2010.

Fahnestock, M., Bindschadler, R., Kwok, R., and Jezek, K.: Greenland Ice Sheet surface properties and ice dynamics from ERS-1 SAR imagery. Science, 262, 1530-1534. https://doi.org/10.1126/science.262.5139.1530, 1993.

Forster, R. R., Box, J. E., Van Den Broeke, M. R., Miège, C., Burgess, E. W., Van Angelen, J. H., Lenaerts, J. T. M., Koenig, L. S., Paden, J., Lewis, C., Gogineni, S. P., Leuschen, C., and McConnell, J. R.: Extensive liquid meltwater storage in firn within the Greenland Ice Sheet, Nat. Geosci., 7, 95–98, https://doi.org/10.1038/ngeo2043, 2014.

Fountain, A. G., and Walder, J. S.: Water flow through temperate glaciers. Rev. of Geophys., 36, 299-328, https://doi.org/10.1029/97RG03579, 1998.

Freilich, M. H., Long, D. G., and Spencer, M. W.: SeaWinds: A scanning scatterometer for ADEOS-II science overview, Proc. IEEE, 1994, 960-963, https://doi.org/10.1109/IGARSS.1994.399313, 1994.
Franco, B., Fettweis, X., and Erpicum, M.: Future projections of the Greenland ice sheet energy balance driving the surface melt, The Cryosphere, 7, 1–18, https://doi.org/10.5194/tc-7-1-2013, 2013

Goward, S. N., Masek, J. G., Williams, D. L., Irons, J. R., and Thompson, R. J.: The Landsat 7 mission: Terrestrial research and applications for the 21st century. Remote Sensing of Environment, 78, 3-12. https://doi.org/10.1016/S0034-4257(01)00262-0, 2001.
Hall, D. K., and DiGirolamo, N.: Multilayer Greenland Ice Surface Temperature, Surface Albedo, and Water Vapor from MODIS, Version 1, NASA National Snow and Ice Data Center Distributed Active Archive Center, https://doi.org/10.5067/7THUWT9NMPDK, 2019.

Hall, D. K., Comiso, J. C., Digirolamo, N. E., Shuman, C. A., Key, J. R., and Koenig, L. S.: A satellite-derived climate-quality data record of the clear-sky surface temperature of the Greenland Ice Sheet, J. Clim., 25, 4785–4798, https://doi.org/10.1175/JCLI-D-11-00365.1, 2012.

Hanna, E., Navarro, F. J., Whitehouse, P. L., Zwally, H. J., Pattyn, F., Domingues, C. M., Fettweis, X., Ivins, E. R., Nicholls, R. J., Ritz, C., Smith, B., and Tulaczyk, S.L: Ice-sheet mass balance and climate change, Nature, 498, 51-59, https://doi.org/10.1038/nature12238, 2013.

Haran, T., Bohlander J., Scambos T., Painter, T., and Fahnestock, M.: MEaSUREs MODIS Boulder, Colorado USA. NASA National Snow and Ice Data Center Distributed Active Archive Center, https://doi.org/10.5067/9ZO79PHOTYE5, 2018.

Harper, J., Humphrey, N., Pfeffer, W. T., Brown, J., and Fettweis, X.: Greenland ice-sheet contribution to sea-level rise buffered by meltwater storage in firn, Nature, 491, 240–243, https://doi.org/10.1038/nature11566, 2012.

Hicks, B. R., and Long, D. G.: Inferring Greenland melt and refreeze severity from SeaWinds scatterometer data, Int. J. Remote Sensing, 32, 8053-8080, https://doi.org/10.1080/01431161.2010.532174, 2011.

Howat, I.: MEaSUREs Greenland Ice Mapping Project (GIMP) Land Ice and Ocean Classification Mask, Version 1, NASA National Snow and Ice Data Center Distributed Active Archive Center, https://doi.org/10.5067/B8X58MQBFUPA, 2017.

Howat, I., Negrete, A., and Smith, B.: MEaSUREs Greenland Ice Mapping Project (GIMP) Digital Elevation Model, Version 1, NASA National Snow and Ice Data Center Distributed Active Archive Center, doi: https://doi.org/10.5067/NV34YUIXLP9W, 2015.

Howat, I., Negrete, A., and Smith, B.: The Greenland Ice Mapping Project (GIMP) land classification and surface elevation datasets, The Cryosphere, 8, 1509-1518, https://doi.org/10.5194/tc-8-1509-2014, 2014.

Humphrey, N. F., Harper, J. T., and Pfeffer, W. T.: Thermal tracking of meltwater retention in Greenland's accumulation area, J. Geophys. Res., 117, https://doi.org/10.1029/2011JF002083, 2012.

Jezek, K. C., Drinkwater M. R., Crawford, J. P., Bindshandler, R., and Kwok, R.: Analysis of synthetic aperture radar data collected over the southwestern Greenland Ice Sheet. J. of Glaciol, 39, 119-132, https://doi.org/10.1017/S002214300001577X, 1993.

Jezek, K. C., Gogineni, P., and Shanableh, M.: Radar measurements of melt zones on the Greenland Ice Sheet, Geophys. Res. Lett., 21, 33-36, https://doi.org/10.1029/93GL03377, 1994.

Jezek, K. C., Johnson, J. T., Drinkwater, M. R., Macelloni, G., Tsang, L., Aksoy, M., and Durand M.: Radiometric approach for estimating relative changes in intraglacier average temperature, IEEE Trans. Geosci. Remote Sens., 53, 134-143, https://doi.org/10.1109/TGRS.2014.2319265, 2015.

Jezek, K. C., Johnson J. T., Tan S., Tsang L., Andrews, M. J., Brogioni, M., Macelloni, G., Durand, M., Chen, C. C., Belgiovane, D. J., Duan, Y., Yardim, C., Li, H., Bringer, A., Leuski, V., and Aksoy, M.: 500–2000-MHz brightness temperature spectra of the northwestern Greenland Ice Sheet, IEEE Trans. Geosci. Remote Sens., 56, 1485-1496, https://doi.org/10.1109/TGRS.2017.2764381, 2018.

Jones, W. L., Schroeder, L. C., Boggs, D. H., Bracalente, E. M., Brown, R. A., Dome, G. J., Pierson, W. J., and Wentz, F. J.: The SEASAT-A satellite scatterometer: The geophysical evaluation of remotely sensed wind vectors over the ocean: J. Geophys. Res. Oceans, 87, 3297-3317, https://doi.org/10.1029/JC087iC05p03297, 1982.

Joughin, I., Das, S. B., Flowers, G .E., Behn, M. D., Alley, R. B., King, M. A., Smith, B. E., Bamber, J. L., van den Broeke, M. R., and Van Angelen, J. H.: Influence of ice-sheet geometry and supraglacial lakes on seasonal ice-flow variability, The Cryosphere, 7, 1185-1192, https://doi.org/10.5194/tc-7-1185-2013, 2013.

Joughin, I., Das, S. B., King, M. A., Smith, B. E., Howat, I. M., and Moon, T.: Seasonal speedup along the western flank of the Greenland Ice Sheet, Science, 320, 781-783, https://doi.org/10.1126/science.1153288, 2008.

Kerr, Y. H., Waldteufel, P., Wigneron, J., Martinuzzi, J., Font, J., and Berger, M.: Soil moisture retrieval from space: The Soil Moisture and Ocean Salinity (SMOS) mission, IEEE Trans. Geosci. Remote Sens., 39, 1729-1735, https://doi.org/10.1109/36.942551, 2001.

Koenig, L. S., Miège, C., Forster, R. R., and Brucker, L.: Initial in situ measurements of perennial meltwater storage in the Greenland firn aquifer, Geophys. Res. Lett., 41, 81-85, https://doi.org/10.1002/2013GL058083, 2014.

Kuipers Munneke, P. K., Ligtenberg, S. R. M., Van Den Broeke, M. R., Van Angelen, J. H., and Forster, R. R.: Explaining the presence of perennial liquid water bodies in the firn of the Greenland Ice Sheet, Geophys. Res. Lett., 41, 476–483, https://doi.org/10.1002/2013GL058389, 2014.

Le Vine, D. M., Lagerloef, G. S. E., and Torrusio, S. E.: Aquarius and remote sensing of sea surface salinity from space, Proc. IEEE, 98, 688-703, https://doi.org/10.1109/JPROC.2010.2040550, 2010.

Lewis, C., Gogineni, S., Rodriguez-Morales, F., Panzer, B., Stumpf, T., Paden, J., and Leuschen, C.: Airborne fine-resolution UHF radar: An approach to the study of englacial reflections, firn compaction and ice attenuation rates, J. Glaciology, 61, 89-100. https://doi.org/10.3189/2015JoG14J089, 2015.

Long, D. G., Brodzik, M. J., and Hardman M. A.: Enhanced-resolution SMAP brightness temperature image products, IEEE Trans. Geosci. Remote Sens., 57, 4151-4163, https://doi.org/10.1109/TGRS.2018.2889427, 2019.

Long, D. G., and Brodzik, M. J.: Optimum image formation for spaceborne microwave radiometer products, IEEE Trans. Geosci. Remote Sens., 54, 2763-2779. https://doi.org/10.1109/TGRS.2015.2505677, 2016.

Long, D. G., and Daum, D. L.: Spatial resolution enhancement of SSM/I data, IEEE Trans. Geosci. Remote Sens., 36, 407-417, https://doi.org/10.1109/36.662726, 1998.

Long, D. G., and Drinkwater, M. R.: Greenland Ice Sheet surface properties observed by the Seasat-A scatterometer at enhanced resolution, J. Glaciol., 40, 213-230, https://doi.org/10.1017/S0022143000007310, 1994.

Long, D. G., Hardin, P. J., and Whiting, P. T.: Resolution enhancement of spaceborne scatterometer data, IEEE Trans. Geosci. Remote Sens., 31, 700-715, https://doi.org/10.1109/36.225536, 1993.

MacFerrin, M., Machguth, H., van As, D., Charalampidis, C., Stevens, C. M., Heilig, A., Vandecrux, B., Langen, P. L., Mottram, R., Fettweis, X., van den Broeke, M. R., Pfeffer, W. T., Moussavi, M. S., and Abdalati, W.: Rapid expansion of Greenland's low-permeability ice slabs. Nature, 573, 403-407, https://doi.org/10.1038/s41586-019-1550-3, 2019.

Machguth, H. MacFerrin M., van As, D., Box, J. E., Charalampidis, C., Colgan., W., Fausto, R. S., Harro, A. J., Mosley-Thompson, E., and van de Wal, R. S. W.: Greenland meltwater storage in firn limited by near-surface ice formation. *Nat. Clim. Chang*. 6, 390-393, https://doi.org/10.1038/nclimate2899, 2016.

Mätzler, C., and Hüppi, R.: Review of signature studies for microwave remote sensing of snowpacks, Adv. in Space Res., 9, 253-265, https://doi.org/10.1016/0273-1177(89)90493-6, 1989.

Miège, C., Forster, R. R., Brucker, L., Koenig, L. S., Solomon, D.K., Paden, J. D., Box, J. E., Burgess, E. W., Miller, J. Z., McNerney, L., Brautigam, N., Fausto, R. S., and Gogineni, S.: Spatial extent and temporal variability of Greenland firn aquifers detected by ground and airborne radars, J. Geophys. Res. Earth, 121, 2381–2398, https://doi.org/10.1002/2016JF003869, 2016.

Miles, K. E., Willis, I. C., Benedek, C. L., Williamson, A. G., and Tedesco, M.: Toward monitoring surface and subsurface lakes on the Greenland Ice Sheet Using Sentinel-1 SAR and Landsat-8 OLI imagery, Frontiers in Earth Science, 5, 58, https://doi.org/https://doi.org/10.3389/feart.2017.00058, 2017.

Miller, J. Z., Long, D. G., Jezek, K. C., Johnson, J. T., Brodzik, M. J., Shuman, C. A., Koenig, L. S., and Scambos, T. A.: Brief communication: Mapping Greenland's perennial firn aquifers using enhanced-resolution L-band brightness temperature image time series, The Cryosphere, 14, 2809–2817, https://doi.org/10.5194/tc-14-2809-2020, 2020.

Miller, J. Z.: Mapping Greenland's firn aquifers from space using active and passive satellite microwave remote sensing, Ph.D. thesis, Department of Geography, University of Utah, 135 pp., 2019.

Miller, O. L., Solomon, D. K., Miège, C., Koenig, L. S., Forster, R. R., Montgomery, L. N., Schmerr, N., Ligtenberg, S. R. M., Legchenko, A., and Brucker, L.: Hydraulic conductivity of a firn aquifer in southeast Greenland, Front. Earth Sci., 5, https://doi.org/10.3389/feart.2017.00038, 2017.

Montgomery, L. N., Schmerr, N., Burdick, S., Forster, R. R., Koenig, L., Legchenko, A., Ligtenberg, S., Miège, C., Miller, O. L., and Solomon, D. K.: Investigation of firn aquifer structure in southeastern Greenland using active source seismology, Front. Earth Sci., 5, https://doi.org/10.3389/feart.2017.00010, 2017.

Moon, T., Joughin, I., Smith, B., Broeke, M. R., Berg, W. J., Noël, B., and Usher, M.: Distinct patterns of seasonal Greenland glacier velocity, Geophys. Res. Lett., 41, 7209-7216, https://doi.org/10.1002/2014GL061836, 2014.

Mote, T. L., and Andersen, M. R.: Variations in snowpack melt on the Greenland Ice Sheet based on passive microwave measurements, J. Glaciology, 41, 51-60, https://doi.org/10.1017/S0022143000017755, 1995.

Noël, B., van Kampenhout, L., Lenaerts, J. T. M., van de Berg, W. J, and van den Broeke, M. R.: A 21st century warming threshold for sustained Greenland Ice Sheet mass loss, Geophys. Res. Lett.,, 48(5), https://doi.org/10.1029/2020GL090471, 2021.

Noël, B., van de Berg, Willem Jan, Lhermitte, S. L. M., and van den Broeke, Michiel R.: Rapid ablation zone expansion amplifies north Greenland mass loss, Sci. Adv, 5, eaaw0123, https://doi.org/10.1126/sciadv.aaw0123, 2019.

Noël, B., van de Berg, W. J., van Wessem, J. M., van Meijgaard, E., van As, D., Lenaerts, J. T. M., Lhermitte, S., Kuipers Munneke, P., Smeets, C. J. P. P., van Ulft, L. H., van de Wal, R. S. W., and van den Broeke, M. R.: Modelling the climate and surface mass balance of polar ice sheets using RACMO2 – Part 1: Greenland (1958–2016), The Cryosphere, 12, 811–831, https://doi.org/10.5194/tc-12-811-2018, 2018.

Nghiem, S. V., Hall, D. K., Mote, T. L., Tedesco, M., Albert, M. R., Keegan, K., Shuman, C. A., DiGirolamo, N. E., & Neumann, G.: The extreme melt across the Greenland Ice Sheet in 2012, Geophys. Res. Lett.,, 39, https://doi.org/10.1029/2012GL053611, 2003

Nghiem, S. V., Hall, D. K., Mote, T. L., Tedesco, M., Albert, M. R., Keegan, K., Shuman, C. A., DiGirolamo, N.E., and Neumann, G.: The extreme melt across the Greenland Ice Sheet in 2012, Geophys. Res. Lett., 39, L20502, https://doi.org/10.1029/2012GL053611, 2012.

Paden, J., Li, J., Leuschen C., F. Rodriguez-Morales, F., and Hale, R.: IceBridge Accumulation Radar L1B Geolocated Radar Echo Strength Profiles, Version 2, NASA National Snow and Ice Data Center Distributed Active Archive Center, https://doi.org/10.5067/0ZY1XYHNIQNY, 2014, updated 2018.

Partington, K. C.: Discrimination of glacier facies using multi-temporal SAR data. J. Glaciol., 44, 42-53. https://doi.org/10.3189/S0022143000002331, 1998.

Pfeffer, W. T., Meier, M. F., and Illangasekare, T. H.: Retention of Greenland runoff by refreezing: Implications for projected future sea level change. J. Geophys. Res. Oceans, 96, 22117-22124, https://doi.org/10.1029/91JC0250, 1991.

Pfeffer, W. T., and Humphrey, N.F.: Determination of timing and location of water movement and ice-layer formation by temperature measurements in sub-freezing snow, J. Glaciol., 42, 292-304, https://doi.org/10.1017/S0022143000004159, 1996.

Piepmeier, J. R., et al.: SMAP L-band microwave radiometer: Instrument design and first year on orbit. IEEE Trans. Geosci. Remote Sens, 55, 1954-1966, https://doi.org/10.1109/TGRS.2016.2631978, 2017.

Poinar, K., Joughin, I., Lilien, D., Brucker, L., Kehrl, L., and Nowicki, S.: Drainage of southeast Greenland firn aquifer water through crevasses to the bed. Front. Earth Sci., https://doi.org/10.3389/feart.2017.00005, 2017.

Poinar, K., Dow, C. F., and Andrews, L. C.: Long-term support of an active subglacial hydrologic system in southeast Greenland by firn aquifers. Geophys. Res. Lett., 46, 4772-4781, https://doi.org/10.1029/2019GL082786, 2019.

Rignot, E.: Backscatter model for the unusual radar properties of the Greenland Ice Sheet, J. Geophys. Res. Planets, 100, 9389–9400, https://doi.org/10.1029/95JE00485, 1995.

Rignot, E. J., Ostro, S. J., Van Zyl, J., and Jezek, K. C.: Unusual radar echoes from the Greenland Ice Sheet, Science, 261, 1710-1713, https://doi.org/10.1126/science.261.5129.171, 1993.

Rodriguez-Morales, F., et al.: Advanced multi-frequency radar instrumentation for polar research, IEEE Trans. Geosci. Remote Sens., 52, 2824-2842, https://doi.org/10.1109/TGRS.2013.2266415, (2014).

Schröder L., Neckel N., Zindler R., Humbert A.: Perennial supraglacial lakes in northeast Greenland observed by polarimetric SAR, Remote Sensing, 12, 2798, https://doi.org/10.3390/rs12172798 (2020).

Shuman, C. A., Hall, D. K., DiGirolamo, N. E., Mefford T. K., and Schnaubelt, M. J.: Comparison of near-surface air temperatures and MODIS ice-surface temperatures at Summit, Greenland (2008–2013), J. Appl. Meteor. Climatol., 53, 2171-2180, https://doi.org/10.1175/JAMC-D-14-0023.1, 2014.

Steffen, K., Nghiem, S. V., Huff, R., and Neumann, G.: The melt anomaly of 2002 on the Greenland Ice Sheet from active and passive microwave satellite observations. Geophys. Res. Lett., 31, L2040, https://doi.org/10.1029/2004GL020444, 2004.

Stevens, L. A., Behn, M. D., McGuire, J. J., Das, S. B., Joughin, I., Herring, T., Shean, D. E., and King, M. A.: Greenland supraglacial lake drainages triggered by hydrologically induced basal slip, Nature, 522, 73-76. https://doi.org/10.1038/nature14480, 2015.

Swift, C. T., Hayes, P. S., Herd, J. S., Jones, W. L., and Delnore, V. E.: Airborne microwave measurements of the southern Greenland Ice Sheet, J. Geophys. Res. Solid Earth, 90, 1983-1994, https://doi.org/10.1029/JB090iB02p01983, 1985.

Tedesco, M., and Fettweis, X.: Unprecedented atmospheric conditions (1948–2019) drive the 2019 exceptional melting season over the Greenland Ice Sheet, The Cryosphere, 14, 1209-1223, https://doi.org/10.5194/tc-14-1209-2020, 2020.

Tedesco, M., Mote, T., Fettweis, X., Hanna, E., Jeyaratnam, J., Booth, J. F., Datta, R., and Briggs, K.: Arctic cut-off high drives the poleward shift of a new Greenland melting record, Nature Commun., 7, 11723-11723, https://doi.org/10.1038/ncomms11723 1985, 2016.

Tedesco, M., Fettweis, X., van den Broeke, M. R., van de Wal, R. S. W., Smeets, C. J. P. P., van de Berg, W. J., Serreze, M. C., and Box, J. E.: The role of albedo and accumulation in the 2010 melting record in Greenland, Environ. Res. Lett, 6, 014005, https://doi.org/10.1088/1748-9326/6/1/014005, 2011.

Tedesco, M., Serreze, M., and Fettweis, X.: Diagnosing the extreme surface melt event over southwestern Greenland in 2007. The Cryosphere, 2, 159-166. https://doi.org/10.5194/tc-2-159-2008, 2008.

Tiuri, M. E., Sihvola, A. H., Nyfors, E. G., Hallikaiken, M. T.: The complex dielectric constant of snow at microwave frequencies, IEEE J. Ocean Eng, 9, 377-382, https://doi.org/10.1109/JOE.1984.1145645, 1984.

Tsai, W., Nghiem, S. V., Van Zyl, J. J.: SeaWinds scatterometer on QuikSCAT mission and the emerging land and ocean applications, Proc. SPIE 4152, https://doi.org/10.1117/12.410586, 2000.

Trusel, L. D., Das, S. B., Osman, M. B., Evans, M. J., Smith, B. E., Fettweis, X., McConnell, J. R., Noël, B. P. Y., and van den Broeke, M. R.: Nonlinear rise in Greenland runoff in response to post-industrial Arctic warming, Nature, 564, 104-108, https://doi.org/10.1038/s41586-018-0752-4, 2018.

Turton, J. V., Hochreuther, P., Reimann, N., and Blau, M. T.: The distribution and evolution of supraglacial lakes on the 79° N Glacier (northeast Greenland) and interannual climatic controls, The Cryosphere Discuss, https://doi.org/10.5194/tc-2021-45, in review, 2021.

Ulaby, F. T., Long, D. G., Blackwell, W. J., Elachi, C., Fung, A. K., Ruf, C., Sarabandi, C., Zebker, H. A., Van Zyl, J.: Microwave radar and radiometric remote sensing, University of Michigan Press, Ann Arbor, 2014.

van den Broeke, M. R., Enderlin, E. M., Howat, I. M., Kuipers Munneke, P., Noël, B. P. Y., van de Berg, W. J., van Meijgaard, E., and Wouters, B.: On the recent contribution of the Greenland ice sheet to sea level change, The Cryosphere, 10, 1933–1946, https://doi.org/10.5194/tc-10-1933-2016, 2016.

van der Veen, C. J.: Fracture propagation as means of rapidly transferring surface meltwater to the base of glaciers, Geophys. Res. Lett., 34, L01501, https://doi.org/10.1029/2006GL028385, 2005.

Wessel, P., and Smith, W. H. F.: A global, self-consistent, hierarchical, high-resolution shoreline database, J. Geophys. Res., 101, 8741–8743, https://doi.org/10.1029/96JB00104, 1996.

Zabel, I. H. H., Jezek, K. C., Baggeroer, P. A., and Gogineni, S. P: Ground-based radar observations of snow stratigraphy and melt processes in the percolation facies of the Greenland Ice Sheet, Ann. Glaciol., 21, 40-44. https://doi.org/10.3189/S0260305500015573, 1995.

Zwally, H. J., Abdalati, W., Herring, T., Larson, K., Saba, J., and Steffen, K.: Surface melt-induced acceleration of Greenland Ice Sheet flow, Science, 297, 218-222, https://doi.org/10.1126/science.1072708, 2002.

Zwally, J. H.: Microwave emissivity and accumulation rate of polar firn, J. Glaciol., 18, 195-215, https://doi.org/10.1017/S0022143000021304, 1977.

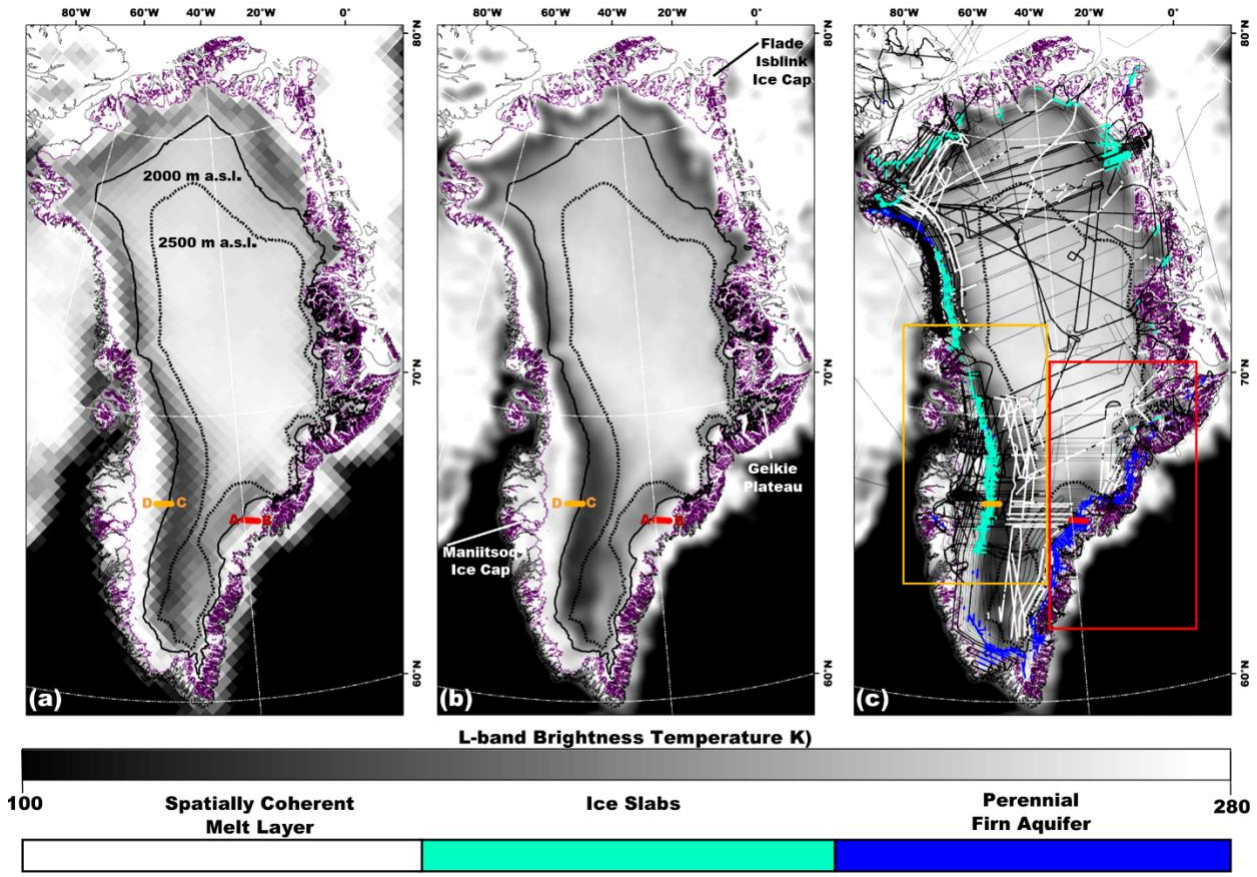

Figure 1

(a) Gridded (25 km gridding, 30 km effective resolution), and (b) enhanced-resolution (3.125 km gridding, 18 km effective resolution) L-band T_V^B imagery generated using observations collected 15 April 2016 by the microwave radiometer on the SMAP satellite during the evening orbital pass interval over Greenland (Long et al., 2019) overlaid with the 2000 m a.s.l. contour (black line), and the 2500 m a.s.l. contour (dotted black line; Howat et al., 2014); the ice sheet extent (purple line; Howat et al., 2014); and the coastline (black peripheral line; Wessel and Smith, 1996). (c) SMAP enhanced-resolution L-band T_V^B imagery overlaid with AR- and MCoRDS-derived 2010-2017 perennial firn aquifer (blue shading; Miège et al., 2016), 2010-2014 ice slab (cyan shading; MacFerrin et al., 2019), and 2012 spatially coherent melt layer (white shading; Culberg et al., 2021) detections along OIB flight lines (black interior lines); zoom areas over south eastern Greenland (red box; Fig. 2a), and south western Greenland (orange box; Fig. 2b); and AR radargram transect A-B (red line; Fig. 3a) and C-D (orange line; Fig. 3b).

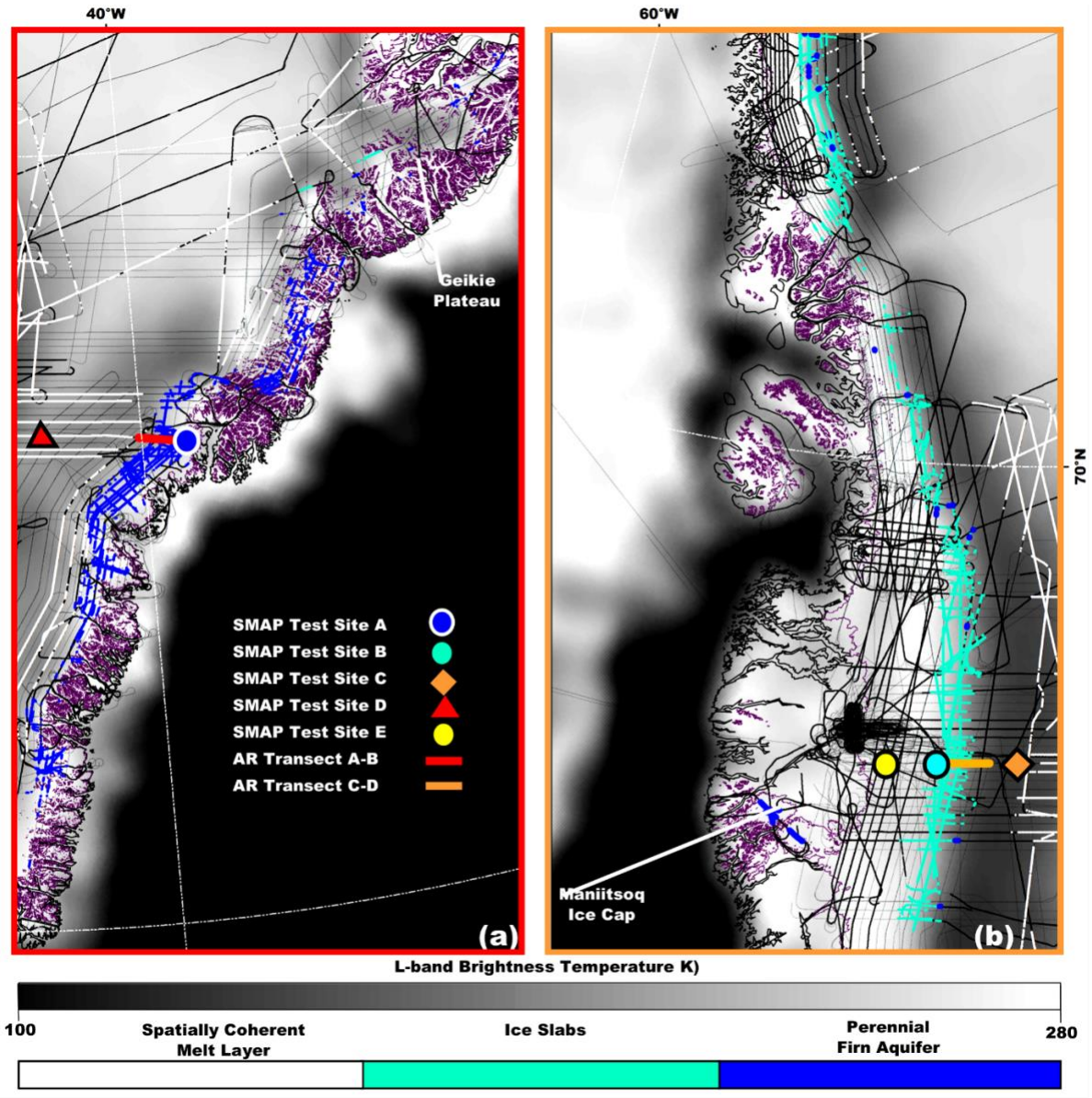

Figure 2

Enhanced-resolution (3.125 km gridding, 30 km effective resolution) L-band T_V^B imagery generated using observations collected 15 April 2016 by the microwave radiometer on the SMAP satellite during the evening orbital pass interval over (a) south eastern Greenland (red box, Fig. 1c), and (b) south western Greenland (orange box, Fig. 1c,) (Long et al., 2019) overlaid with the ice sheet extent (purple line; Howat et al., 2014); the coastline (black peripheral line; Wessel and Smith, 1996); the AR- and MCoRDS-derived 2010-2017 perennial firn aquifer (blue shading; Miège et al., 2016), 2010-2014 ice slab (cyan shading; MacFerrin et al., 2019), and 2012 spatially coherent melt layer (white shading; Culberg et al., 2021) detections along OIB flight lines (black interior lines); AR transect A-B (red line; Fig. 3a), and C-D (orange line; Fig. 3b); and SMAP Test Site A (blue circle; Fig. 4a), B (cyan circle; Fig. 4b), C (orange diamond; Fig. 4c), D (red triangle; Fig. 4d), and E (yellow circle; Fig. 4e).

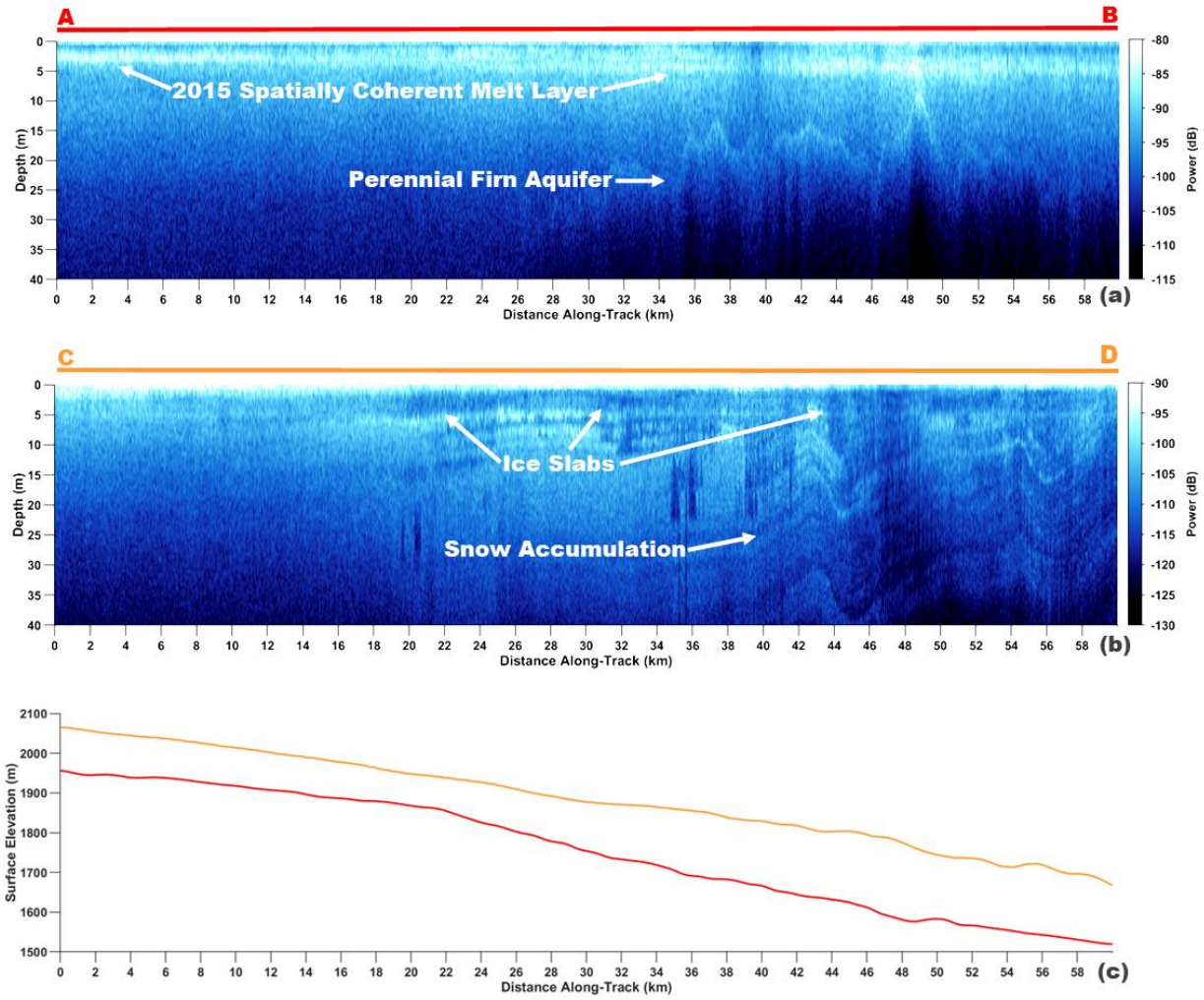

Figure 3

AR transect (a) A-B (red line, Fig. 2a) collected on 22 April 2017, and (b) C-D (orange line, Fig. 2b) collected on 5 May 2017 (Rodriguez-Morales et al, 2014). (c) AR transect A-B (red line), and C-D (orangle line) elevation profiles. The exceptionally bright upper surface-parallel reflector in (a) is a spatially coherent melt layer. The bright lower reflector in (a) is the upper surface of meltwater stored within a perennial firn aquifer. The thick dark surface-parallel regions of low-reflectivity in (b) are ice slabs. The alternating sequences of bright and dark surface-parallel reflectors in (b) are seasonal snow accumulation layers.

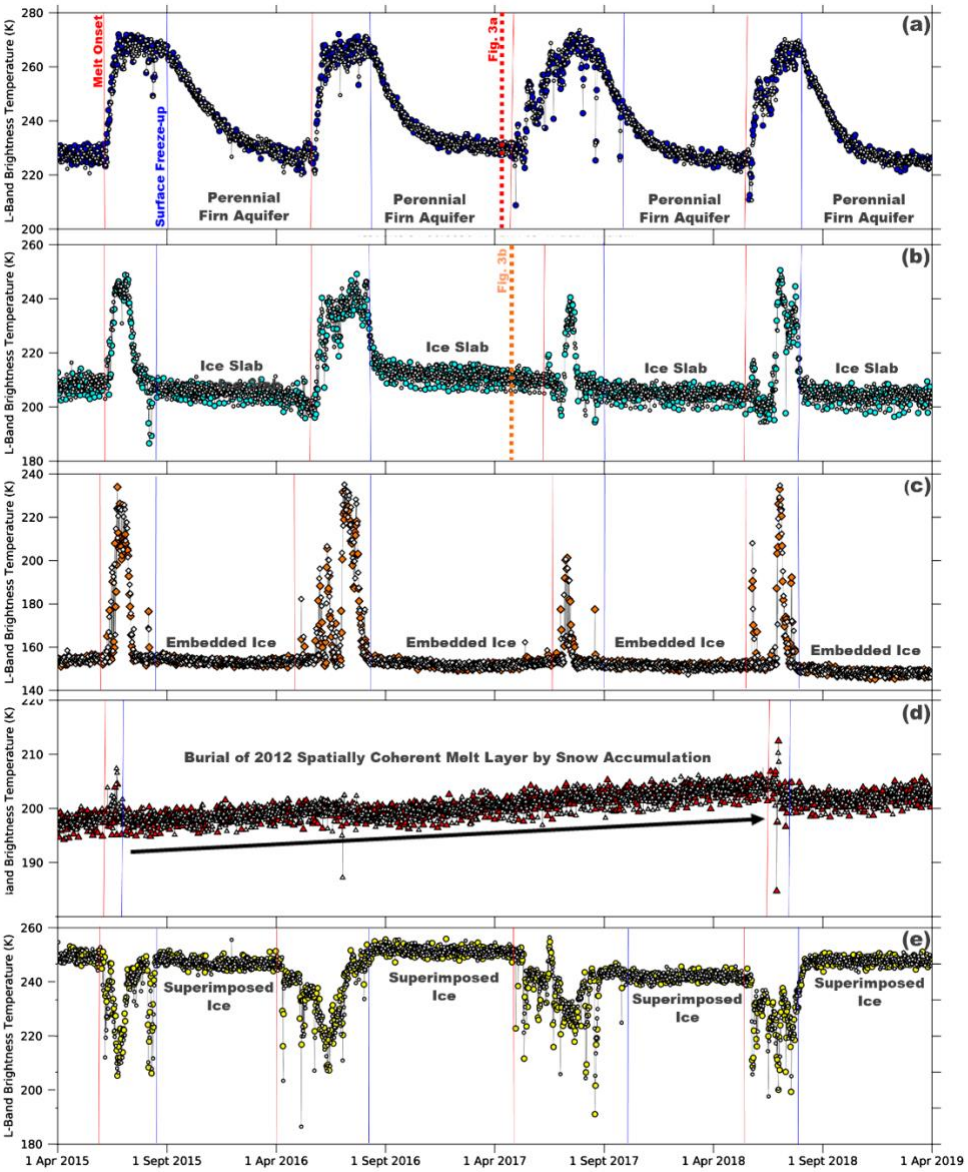

Figure 4

Temporal L-band signatures that alternate morning (white symbols) and evening (colored symbols) orbital pass interval enhanced-resolution T_V^B generated using observations collected over the GrIS by the microwave radiometer on the SMAP satellite (Long et al., 2019) over (a) SMAP Test Site A (blue circles; Fig. 2a), (b) B (cyan circles; Fig. 2b), (c) C (orange diamonds; Fig 2b), (d) D (red triangles; Fig. 2a), and (e) E (yellow circles; Fig. 2b). Melt onset (red lines) and surface freeze-up (blue lines) dates derived from thermal infrared T^B collected by MODIS on the Terra and Aqua satellites (Hall et al, 2012). AR transect A-B (red dashed line; Figs. 3a) collected on 22 April 2017, and C-D (orange dashed line; Fig. 3b) collected on 5 May 2017.

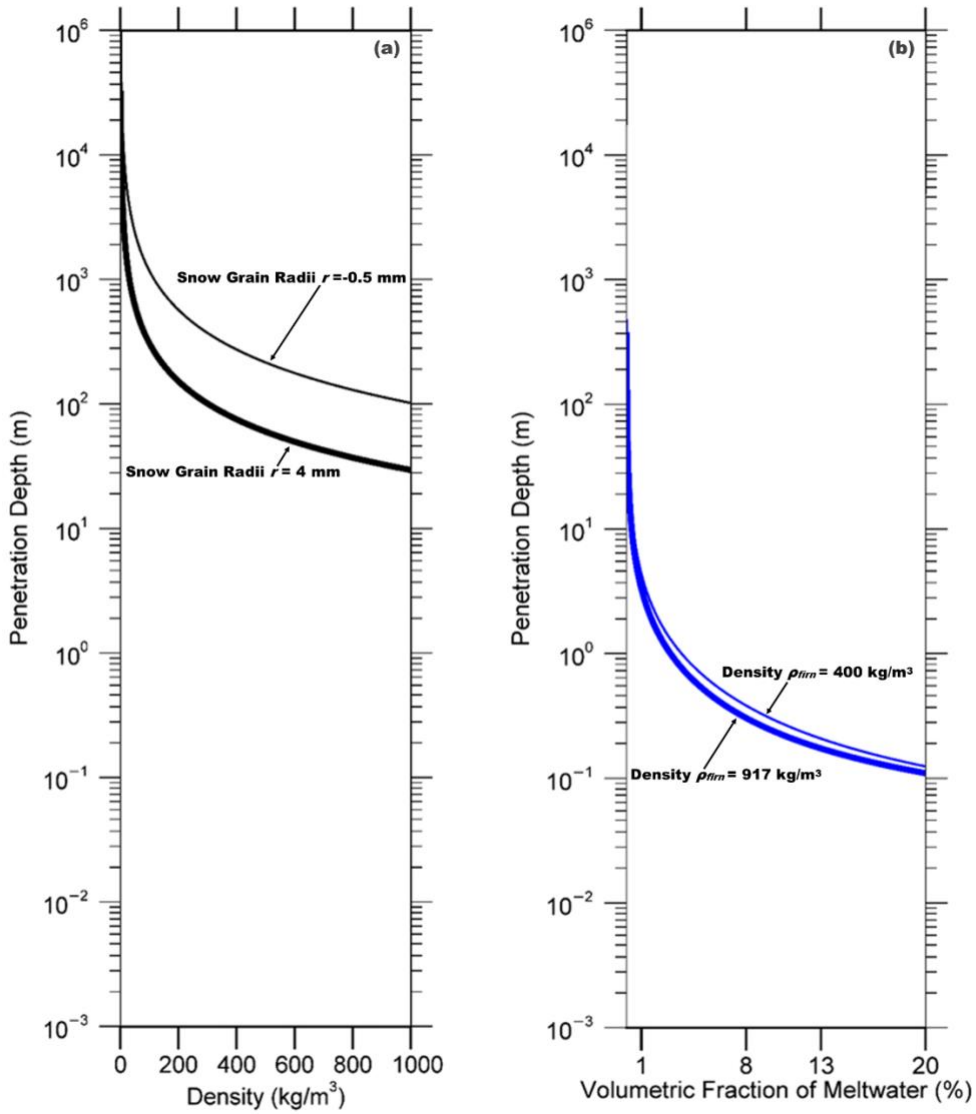

Figure 5

Theoretical L-band penetration depths for of uniform layer of (a) refrozen, and (b) water-saturated firn. Penetration depths $\left(\frac{1}{\kappa_s+\kappa_a}\right)$ *are calculated as a function of the Raleigh scattering coefficient (*κ_s*; Eq. 8), and the absorption coefficient (*κ_a*; Eq. 10). The complex dielectric constant is calculated using the empirically derived models described in Tiuri et al., (1984). Refrozen firn penetration depths are calculated as a function of firn density (*ρ_{firn}*), and the curves are plotted for snow grain radii (*r*) set to* r*=0.5 mm (upper curve), and* r*=4 mm (lower curve). Water-saturated firn penetration depths are calculated as a function of the volumetric fraction of meltwater (*m_v*), and the curves are plotted for firn density set to* ρ_{firn}*=400 kg/m³ (upper curve), and* ρ_{firn}*=917 kg/m³ (lower curve). Given the complexity of modeling embedded ice structures, they are excluded from the penetration depth calculation. Increases in the volumetric fraction of embedded ice within the firn will result in an increase in volume scattering, which will decrease and compress the distance between the penetration depth curves for both refrozen and water-saturated firn.*

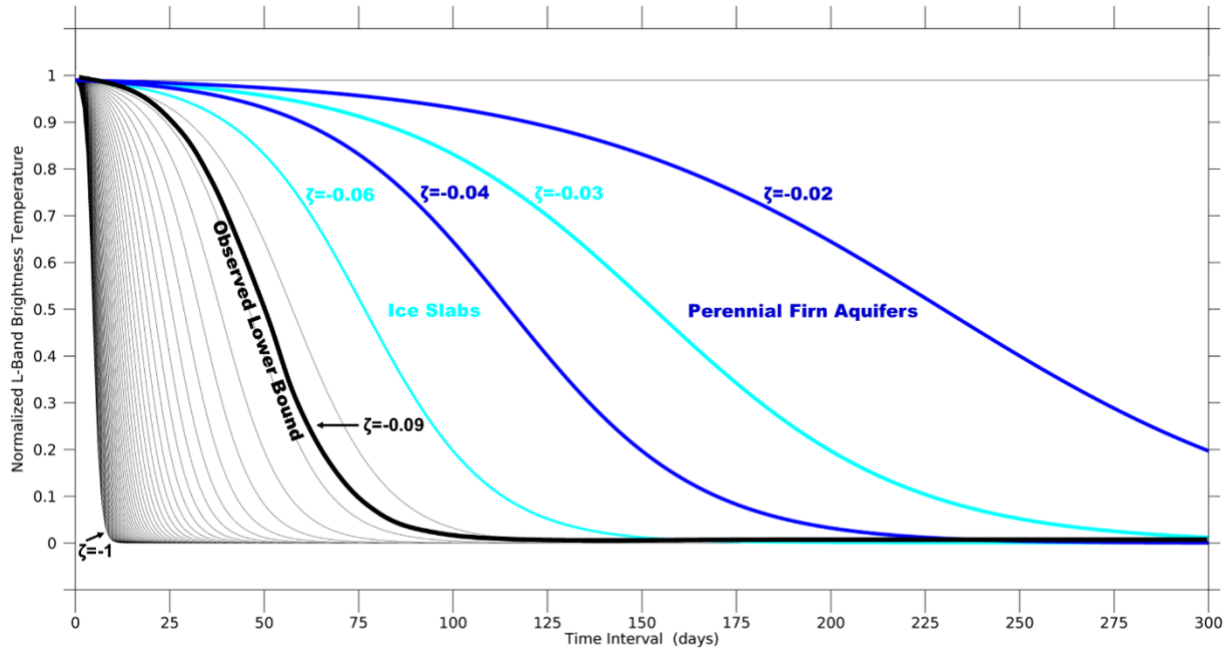

Figure 6

Example set of simulated sigmoidal curves that represent our model of the exponentially decreasing temporal L-band signatures predicted over the percolation facies. The initial normalized vertically-polarized L-band brightness temperature was fixed at a value of $T_{V,N}^{B}(t_{max})$ *= 0.99, and the time interval was set to a value of* $t \in [\, t_{max}, t_{min}]$ *= 300 observations. The refreezing rate parameter was set to values between* $\zeta = [\, -1, 0\,]$ *incremented by steps of 0.02. The blue lines correspond to the interval* $\zeta \in [\, -0.04, -0.02\,]$ *and produce curves similar to those observed over perennial firn aquifer areas. The cyan lines correspond to the interval* $\zeta \in [-0.06, -0.03\,]$ *and produce curves similar to those observed over ice slab areas. The black line is the observed lower bound (*ζ *= -0.09) of the refreezing rate parameter of partitioned* T_{V}^{B} *time series iteratively fit to the sigmoid function (Section 2.3.4).*

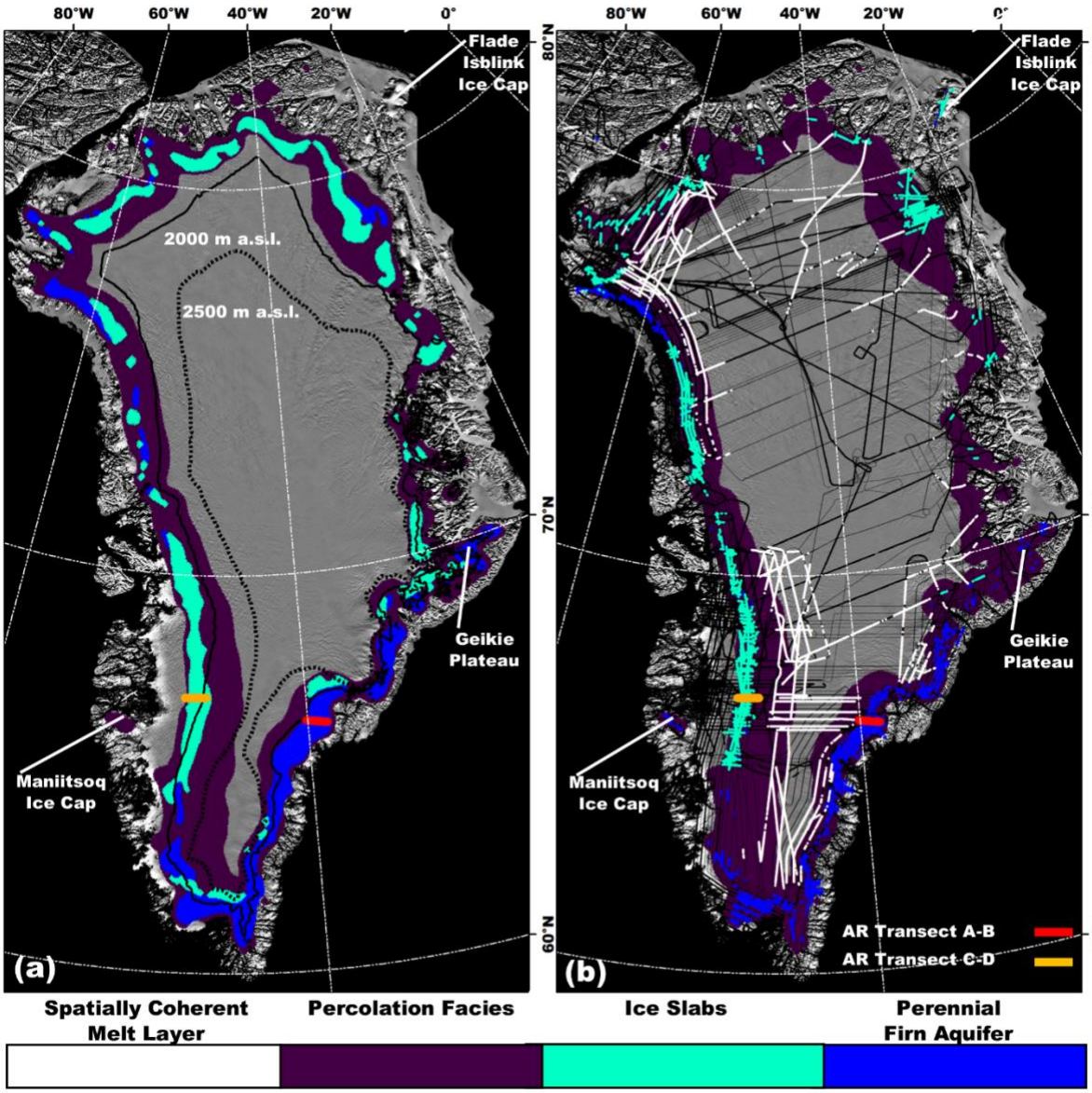

Figure 7

(a) SMAP-derived perennial firn aquifer (blue shading), ice slab (cyan shading), and percolation facies (purple shading) extents (2015-2019) generated by the adapted empirical algorithm; and the 2000 m a.s.l. contour (black line), and the 2500 m a.s.l. contour (black dotted line; Howat et al., 2014) overlaid on the 2015 MODIS Mosaic of Greenland (MOG) image map (Haran et al., 2018). (b) SMAP-derived extents are overlaid with AR- and MCoRDS-derived 2010-2017 perennial firn aquifer (blue shading; Miège et al., 2016), 2010-2014 ice slab (cyan shading; MacFerrin et al., 2019), and 2012 spatially coherent melt layer (white shading; Culberg et al., 2021) detections along OIB flight lines (black interior lines); and AR transect A-B (red line; Fig. 3a), and C-D (orange line; Fig. 3b).

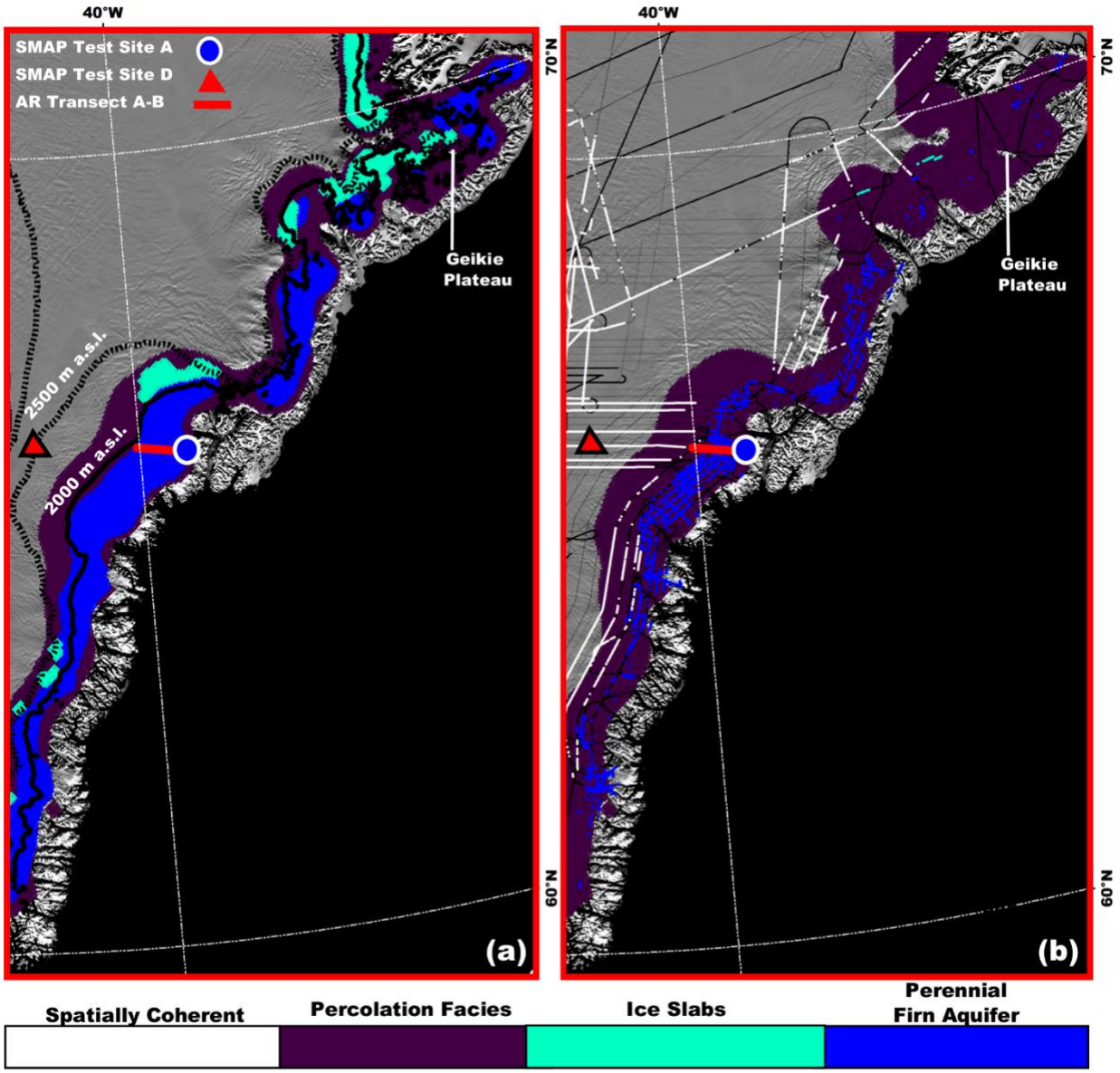

Figure 8

The SMAP-derived perennial firn aquifer (blue shading), ice slab (cyan shading), and percolation facies (purple shading) extents (2015-2019) generated by the adapted empirical algorithm over south eastern Greenland (red box; Fig. 1c); and the 2000 m a.s.l. contour (black line), and the 2500 m a.s.l. contour (black dotted line; Howat et al., 2014) overlaid on the 2015 MODIS MOG image map (Haran et al., 2018). (b) The SMAP-derived percolation facies extent is overlaid with AR- and MCoRDS-derived 2010-2017 perennial firn aquifer (blue shading; Miège et al., 2016), 2010-2014 ice slab (cyan shading; MacFerrin et al., 2019), and 2012 spatially coherent melt layer (white shading; Culberg et al., 2021) detections along OIB flight lines (black lines); AR transect A-B (red line; Fig. 3a); and SMAP Test Site A (blue circle; Fig. 4a), and D (red triangle; Fig 4d).

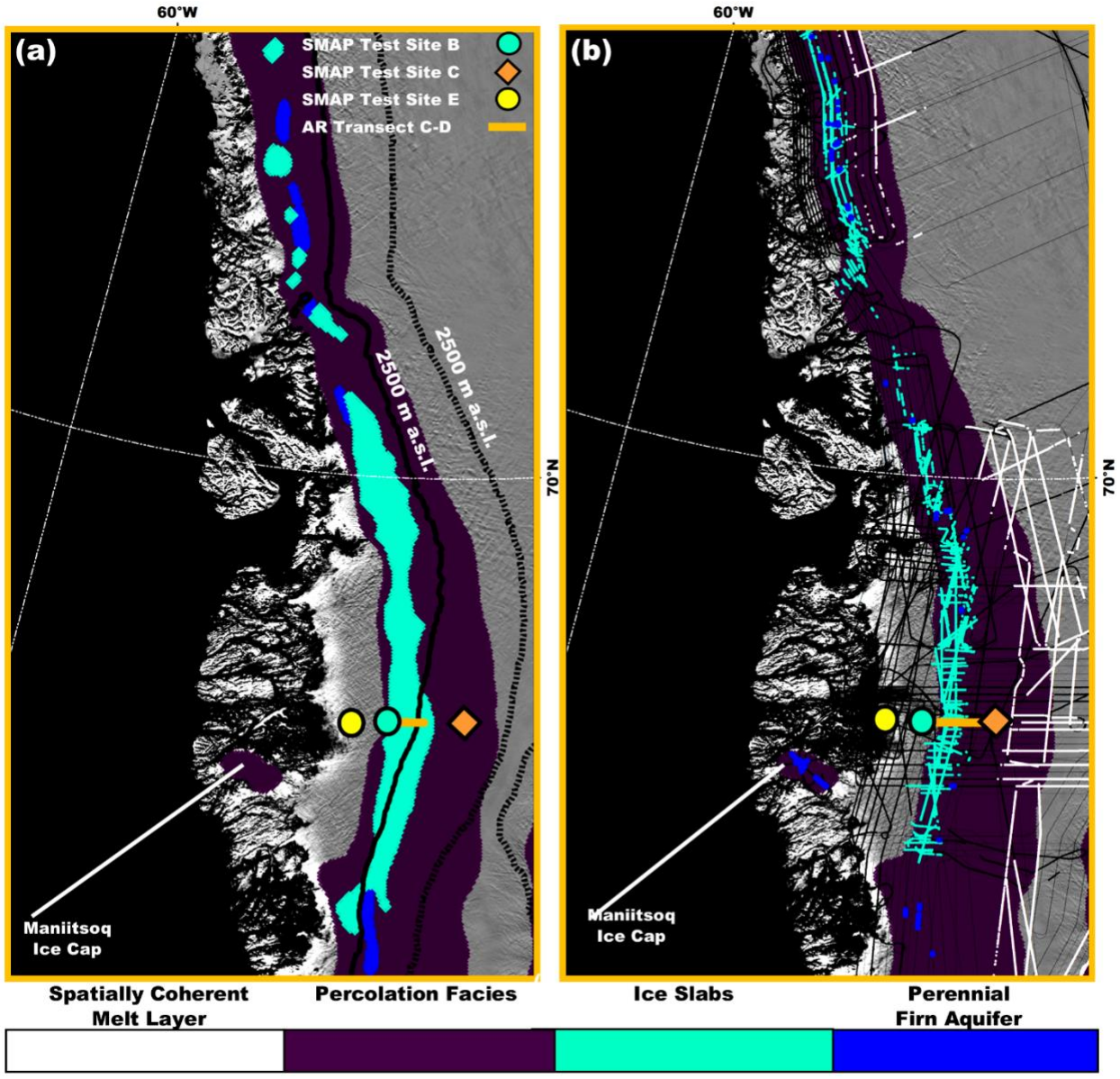

Figure 9

(a) SMAP-derived perennial firn aquifer (blue shading), ice slab (cyan shading), and percolation facies (purple shading) extents (2015-2019) generated by the adapted empirical algorithm over south western Greenland (orange box; Fig. 1c); and the 2000 m a.s.l. contour (black line), and the 2500 m a.s.l. contour (black dotted line; Howat et al., 2014) overlaid on the 2015 MODIS MOG image map (Haran et al., 2018). (b) SMAP-derived percolation facies extent is overlaid with AR- and MCoRDS-derived 2010-2017 perennial firn aquifer (blue shading; Miège et al., 2016), 2010-2014 ice slab (cyan shading; MacFerrin et al., 2019), and 2012 spatially coherent melt layer (white shading; Culberg et al., 2021) detections along OIB flight lines (black interior lines); AR transect C-D (orange line; Fig. 3b); and SMAP Test Site B (cyan circle; Fig. 4b), C (orange diamond; Fig. 4c), and E (yellow circle; Fig. 4e).

Table 1.

MODIS-derived total number of days in the melting and freezing seasons; SMAP-derived maximum vertically-polarized L-band brightness temperature ($T^B_{V,max}$); minimum vertically-polarized L-band brightness temperature ($T^B_{V,min}$); time scale scales of exponential decrease following the surface freeze-up date for perennial firn aquifer, ice slab, percolation facies, dry snow facies, and wet snow facies areas.

	Melting Season (days)	Freezing Season (days)	$T^B_{V,max}$ (K)	$T^B_{V,min}$ (K)	Exponential Decrease (time scale)
Perennial Firn Aquifers	75 - 100	265 - 290	200 - 275	180 – 250	weeks – months
Ice Slabs	60 -90	275 - 305	170 - 260	130 – 240	days - weeks
Percolation Facies	1 - 60	305 - 364	150 - 200	130 – 220	days
Dry Snow Facies	-	365	200 - 240	200 – 240	-
Wet Snow Facies	90 - 120	245 - 275	230 - 250	230 – 250	-

Table 2.

SMAP-derived calibration parameter intervals used for mapping perennial firn aquifer and ice slab extents.

	ξ	$T_{V,max}^{B}$ (K)	$T_{V,min}^{B}$ (K)	ζ
Perennial Firn Aquifers	0.2 – 4	200 – 275	180 – 250	-0.04 – -0.02
Ice Slabs	0.1 – 2	170 – 260	130 – 240	-0.06 – -0.03

Table 3.

Interannual variability in SMAP-derived perennial firn aquifer and ice slab extents.

	Perennial Firn Aquifers (km^2)	Ice Slabs (km^2)
2015-2019	66,000	76,000
2015-2016	63,000	23,000
2016-2017	69,000	48,000
2017-2018	73,000	27,000
2018-2019	70,000	38,000